Observation and modelling of infragravity waves at a large meso-tidal inlet and lagoon

Alexandre Nicolae Lerma, Nico Valentini, Paul Bayle, Xavier Bertin, Florian Ganthy, Arnaud Le Pevedic, Guillaume Detandt, Nadia Sénéchal

Coastal Engineering 193 (2024) 104579

Contents lists available at ScienceDirect

Coastal Engineering

journal homepage: www.elsevier.com/locate/coastaleng

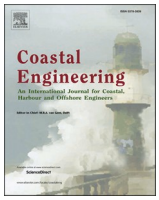

Observation and modelling of infragravity waves at a large meso-tidal inlet and lagoon

Alexandre Nicolae Lerma [a,*], Nico Valentini [a], Paul Bayle [a,b,1], Xavier Bertin [c], Florian Ganthy [b], Arnaud Le Pevedic [b,d], Guillaume Detandt [d], Nadia Sénéchal [d]

[a] BRGM Direction Nouvelle-Aquitaine, Pessac, France
[b] Ifremer/LERAR, Arcachon, France
[c] Université La Rochelle/CNRS, UMR 7266 LIENSS, La Rochelle, France
[d] Université de Bordeaux/CNRS, Bordeaux INP, EPOC, UMR 5805, Pessac, France

ARTICLE INFO

Keywords:
IG waves
Total water level
Storm condition
Flood hazard
XBeach model
Arcachon lagoon

ABSTRACT

The role of infragravity waves (IG waves) in beach and dune erosion or in flood hazard has been extensively studied on open beaches. In contrast, the detailed characterization of IG waves and their contribution to the Total Water Level (TWL) along the shore of inlets received little attention so far. In such environment, there is a real lack of *in situ* observations of waves and hydrodynamics conditions at appropriate spatial and temporal coverage to study the role of infragravity (IG) waves (long waves of frequency typically ranging between 0.004 Hz and 0.04–0.05 Hz) on coastal hazards. This contribution is based on field observations collected at the Arcachon Lagoon, a shallow semi-enclosed lagoon connected to the ocean by a large tidal inlet, located in southwest France. Analyses combine observations made at several locations during storm events within the inlet and the lagoon with numerical simulation with the XBeach surfbeat model to explore the spatial variability of IG waves and simulate observed, historical, and idealized storm conditions. The results show that IG waves are substantial during typical winter storms at the inlet and range from $H_{m0} = 0.8$ to over 1 m across the ebb delta and about 0.4–0.6 m in the inner part of the inlet. At the lagoon entrance, IG waves remain substantial (about 0.1–0.2 m) and decrease to a few centimeters at the lagoon shore. The spatial variability and magnitude of IG waves along the inlet coast, simulated for the historical storms, are quite comparable to those observed during classical winter, and do not increase linearly with offshore wave energy. However, both observations and simulations reveal local amplifications of IG waves in the inner part of the inlet, especially along the sheltered coast were IG waves dominate the variance of free surface elevation, reaching about 0.6–0.7 m during common storms and more than 1 m for an extreme storm scenario. A numerical experiment indicates that IG wave reflection from one coast to the other contributes up to 35–40% of the measured IG wave height at a hot spot located along the sheltered coast. Finally, the contribution of IG waves to TWL at the shore on both sides of the inlet has been estimated to be about 0.4–0.6 m for a common storm and 0.6–0.9 m for an extreme scenario, locally peaking at 0.74 and 1.1 m respectively and overpassing the contribution of wave-induced setup. This work provides new insights into the contribution of IG waves to TWL and its implications for overtopping flooding hazard and overwash processes at large inlets, highlighting the need to consider IG waves in Early Warning Systems or hazard mapping for flood prevention plans in these environments.

1. Introduction

Tidal inlets are transitional areas between the ocean and an estuary or a lagoon. They are common coastal environment (Carter and Woodroffe, 1994) and can take very different forms depending on the geological and hydro-sedimentary context (Hayes and FitzGerald, 2013). Large inlets are generally subject to rapid and large geomorphological evolutions (FitzGerald et al., 1984; Orescanin et al., 2016;

* Corresponding author.
E-mail address: a.nicolaelerma@brgm.fr (A. Nicolae Lerma).
[1] **Currently:** Delft University of Technology, Faculty of Civil Engineering and GeoSciences, Department of Hydraulic Engineering, Stevinweg 1, 2628CN, Delft, The Netherlands.

https://doi.org/10.1016/j.coastaleng.2024.104579
Received 16 November 2023; Received in revised form 11 June 2024; Accepted 14 July 2024
Available online 24 July 2024

Velasquez-Montoya et al., 2020; Fortunato et al., 2021) that can affect the adjacent coastline evolution and bathymetry over time scales ranging from one single storm to several decades (Castelle et al., 2018; Burvingt et al., 2022; Fortunato et al., 2021). Often bordered by sand spits and low-lying coasts, inlet shore and connected lagoons are also frequently affected by flood hazards (e.g., Psuty and Ofiara, 2002; Vila-Concejo et al., 2006) due to overflowing or overwashing (or overtopping) along low coastal dunes (or coastal structures). Consequently, these areas of high economic and environmental values are frequently subject to coastal hazards, which is likely to increase with climate change (Duong et al., 2016).

Tidal inlets and associated lagoons are characterized by highly complex hydro-morphodynamics processes resulting from the interaction between rapid water-level changes, tidal currents and waves (Bruun and Gerritsen, 1959; Hayes, 1979) within a system combining shallow platforms, multiple channels and shoals (e.g., Capo et al., 2014). Over the last 15 years, various studies have investigated the effect of short waves (hereafter denoted 'SW') on the hydro-morphodynamics of inlets, for small-sized (Bertin et al., 2009; Dodet et al., 2013), for medium-sized (Olabarrieta et al., 2011; Wargula et al., 2014; Chen et al., 2015; Zippel and Thomson, 2015) and for large-sizes systems (Elias and Hansen, 2013; Lavaud et al., 2020; Fortunato et al., 2021; Mengual et al., 2022). More recently, the contribution of infragravity (hereafter denoted 'IG') waves to the hydro-morphodynamics in tidal inlets started to receive attention (Bertin and Olabarrieta, 2016; Williams and Stacey, 2016; Bertin et al., 2019; Mendes et al., 2020; Melito et al., 2020), but these studies mostly concerned small and shallow inlets, and it is not clear how the findings of these study apply to larger systems.

IG waves are long waves with a frequency typically comprised between 0.004 Hz and 0.04–0.05 Hz and are driven by the presence of groups in the incident SW (0.04–0.05 Hz $< f <$ 0.5 Hz). From the deep ocean to the shoaling zone, IG waves are mostly generated through the bound wave mechanism (Biesel, 1952; Longuet-Higgins and Stewart, 1962), where the divergence of the momentum flux of the SW at the scale of wave groups leads to a depression of the mean water level at the location of the largest SW, and a higher water level at the location of the smallest wave (or between groups). In the shoaling zone, IG waves start to lag behind the antiphase equilibrium of the group forcing (Longuet-Higgins and Stewart, 1962) and further gain energy from the primary waves (List, 1992; Van Leeuwen, 1992; Janssen et al., 2003). As they continue to propagate toward the coast, bathymetry-induced breaking of the SW leads to the destructuring of the SW groups so that IG waves start to be released and propagate as free waves (Elgar et al., 1992; Ruessink et al., 1998). Recent studies conducted in the field (Paniagua-Arroyave et al., 2019) or using numerical models (Li et al., 2020; Liao et al., 2021) also investigated shoal-induced amplification of IG waves in non-breaking conditions and showed the significant amplification due to the resonance between forcing and IG wave (Liao et al., 2021).

The dominant role of IG waves in open beach and dune erosion processes (e.g., Russell, 1993; Ruggiero et al., 2004; Roelvink et al., 2009) as well as in overwashing/overtopping events (e.g., McCall et al., 2010; Muller et al., 2017; Bertin et al., 2018; Nahon et al., 2023) is well documented in the literature. At the shore, IG waves have the potential to induce rapid water level increase, playing a key role on dune erosion through collision regime, temporary overflow and overtopping or overwashing events. Based on field observations, preliminarily results of Bayle et al. (2022) have shown that IG wave energy fluxes increase in the inlet, propagate and maintain a relatively high energy level hundreds of meters into the lagoon. However, the detailed characterization of IG waves along the shore of large inlets and their contribution to the Total Water Level (TWL) where they are suspected to play a major role in erosion and flood hazards has not yet been studied.

In large-scale inlets, logistical constraints (accessibility, dimensions, intensity of hydrodynamics processes and fast morphological changes) limit field measurements. To date, there is a real lack of *in situ* waves and hydrodynamics observations at appropriate spatial and temporal coverage to study the role of IG waves on the morphodynamics and coastal hazards in such environments, especially during high energetic conditions (Mendes et al., 2020).

Process-based numerical models can be used to analyze IG waves behavior in such large-scale environments. Among the different types of models, phase-resolving models offer the key advantage to simulate the development of IG waves and the energy transfers between IG and SW bands (Rijnsdorp et al., 2014; Nicolae Lerma et al., 2017; Fiedler et al., 2018). Yet, such models are too computationally expensive to be applied at the scale of large tidal inlets, as it would require a spatial resolution in the order of a meter over several hundred of kilometer squared. To overcome these difficulties, surfbeat models, where a single-frequency spectral wave model is coupled with a 2DH circulation model, provide good alternatives for such environments. The surfbeat model XBeach, from Roelvink et al. (2009), demonstrated good performance in reproducing IG waves development and propagation in contrasting coastal environments (Lashley et al., 2019; Bertin et al., 2020; de Beer et al., 2021; Mouragues et al., 2021; Nahon et al., 2023). In our study, we use the XBeach model (Roelvink et al., 2009) to complement the analysis of a new dataset obtained during two extensive field campaigns (ARCADE dataset, Nicolae Lerma et al., 2022; Bayle et al., 2022). The data were collected during winter storm conditions at the meso-macro tidal Arcachon inlet and lagoon (located at the south-west Atlantic coast of France).

The paper is structured as follows. Section 2 presents the study site. Section 3 presents the field measurement campaign and dataset used to calibrate the XBeach model and analyze some processes. Section 4 describes the XBeach model set-up, implementation, calibration and validation, as well as the scenarios used for this study (including moderate, highly energetic historical events and an extreme statistical event). Section 5 presents the field observation and simulation results, focusing on the characterization of the spatial variability of the IG waves at several locations in the Arcachon inlet, along the shore of the inlet and the lagoon. Section 6 discusses the physics behind the results using an extra numerical simulation to explore the role of reflection and resonance of IG waves at the shore of the inlet and finally an empirical parametrization based on observations and simulations is proposed in order to estimate the contribution of swash-induced IG wave to TWL at the inner part of the inlet.

2. Study site

The study site is located to the south-west of France, along the Aquitaine Coast (Fig. 1a). The Arcachon inlet is a mixed-energy meso-macro tidal inlet (following the classification proposed by Hayes, 1979), extending 15 km from North to South and 8 km from the ebb delta to the coast. It is backed by a large, shallow semi-enclosed lagoon of approximately 180 km^2 extending 13 km from north to south and 18 km from west to east.

The inlet is currently organized around two main channels and a few intertidal to supratidal banks, composed of fine to coarse-grain sands (Blanchet et al., 2005). Channels are North-South oriented in the inner part of the inlet (flood-tidal delta) and 30–35°N oriented in the central part (intertidal and supratidal banks) and at the ebb-tidal delta. The Northern part of the ebb delta is made up of a wide, shallow platform extending from the Cap Ferret spit (Nahon et al., 2019).

The inside lagoon is characterized by sandy and muddy intertidal flats and marshes covered by marine grass and shaped by an extensive network of tidal channels (Allard et al., 2009). The Arcachon lagoon is

Fig. 1. Location and bathymetric map of the study site, a) Arcachon Lagoon, b) zoom in the inlet. Red points with associated colored number indicate the location of *in situ* hydrodynamic measurements. Aerial view of c) the western intern part of the inlet (Cap Ferret Spit), d) the eastern part (La Teste). Example of flood hazards during storms at the inlet shores e) overflowing during Xynthia storm (02/2010), f) overtopping (March 12, 2021) and the inner lagoon, g) overflowing during Xynthia storm (02/2010).

an important oyster farming area in France (De Montaudouin et al., 1999), and the concentration of this activity has been considered to be one of the main factors in the evolution of the bathymetry within the lagoon (Allard et al., 2009).

The tidal range varies from 0.94 m to 4.93 m with an average of 2.94 m inside the lagoon (Eyrac tide gauge, Dodet et al., 2019), generating tidal currents that can exceed 2 m s^{-1} in the channels (Salles et al., 2015). Rivers inflow has a limited effect on the hydrodynamics of the lagoon, the main sources being limited to flows of less than 50 m^3 s^{-1} in winter and around 10 m^3 s^{-1} in summer (Plus et al., 2009). In comparison, tidal hydrodynamics is largely dominant, with a tidal prism estimated to ($3.5x10^8$) m^3 (Cayocca, 2001). In consequence, the volume of freshwater introduced into the lagoon by continental sources is negligible compared to the volume of seawater (Allard et al., 2009).

The wave climate is referred to as energetic with an annual mean significant wave height (H_s) of 1.8 m and an average peak period (T_p) of 11.5 s, offshore of the Cap Ferret (Cap Ferret Buoy, location 44°39.15′ N; 01°26.8' W, Fig. 1). The maximum monthly-averaged value of $H_s = 2.4$ m is usually observed in January (Castelle et al., 2017). The hourly significant wave height can reach more than $H_s = 8$ m, with $T_p = 20$ s, during winter storms (Nicolae Lerma et al., 2015), and the highest historical record reached more than 10 m (Lavaud et al., 2020). The dominant wave direction is west to north-west, generating a southerly longshore current that can reach 1.5 m s^{-1} along the inlet (Senechal et al., 2013). The longshore sediment transport along the adjacent open coast is around 650 000 m^3/year to the north of the inlet and 550 000 m^3/year to the south (Idier et al., 2013), but with local particularities along the Cap Ferret spit (Nahon et al., 2022) and the southern part of the inlet (Senechal et al., 2013) due to coupled interactions between wave, tide and local bathymetric features.

The shore of the Arcachon Lagoon is very attractive in terms of tourism (Dachary-Bernard and Lyser, 2016; Sacareau, 2018), and alternates between densely and disparately urbanized areas and natural reserves. It totalized 159 111 inhabitants in 2018, mainly located in low-lying areas exposed to flood hazard (Mugica et al., 2016). In many places around the inlet and the lagoon, the coast is protected by dikes and seawalls (Fig. 1d), but some sectors are still bordered by non-engineered low-volume sandy beaches (e.g., along the inner part of the Cap Ferret spit, Fig. 1c).

3. Field data

3.1. Topo-bathymetry survey

In order to obtain a description of the morphological state of the study area, a total of 955 500 soundings (over a period of 1 year, necessary to cover the domain with high resolution) were collected by the SIBA (*Syndicat Intercommunale du Bassin d'Arcachon*) between spring 2019 and autumn 2020 in the lagoon, and by the DDTM33 (*Direction Departmentale des Territoires et de la Mer*) during a one-week campaign in the inlet in spring 2020. To build a sea-land continuum topo-bathymetric model covering the entire study area, these data were merged with offshore bathymetric soundings (from 50 to 25 m deep) and with topographic LiDAR data collected in 2016. Based on this coverage, a 10 m spatial-resolution digital bathymetry was produced (Fig. 1a). Hereinafter, all topo-bathymetric information are presented relative to the official levelling network in mainland France (NGF/IGN69).

3.2. In situ measurements

Wave and current data were collected during two extensive *in situ* field campaigns conducted in winter 2021 and winter 2022 as part of the ARCADE research project (Nicolae Lerma et al., 2022). Several types of instruments were deployed (Fig. 2) at locations shown in Fig. 1 (similar protocol and location for the two campaigns). The deployed instruments were: a Nortek AWAC (point 1), three ADCP Nortek Signature (point 113, 115, 5), a Nortek Aquadopp (point 112), an ADCP RDI Sentinel (point 4), an RBR soloD pressure transducers (point 114, 11) and an RBR soloWave (point 18). The measurement characteristics for each location are specified in Table 1.

The measurement time window extends over a period of one month and a half in 2021 and one month in 2022 (Nicolae Lerma et al., 2022). In this study, only the measurements taken during two ten-day periods are presented. The first period includes a storm event and the second one a cluster 3 storms (see Fig. 3a and b). The use of these data is twofold: (i) to describe the waves characteristics occurring during the field campaigns; (ii) to calibrate and validate the XBeach model and analyze IG waves behavior (observations and simulations) during the storm peaks (red dashed rectangle in Fig. 3a and b).

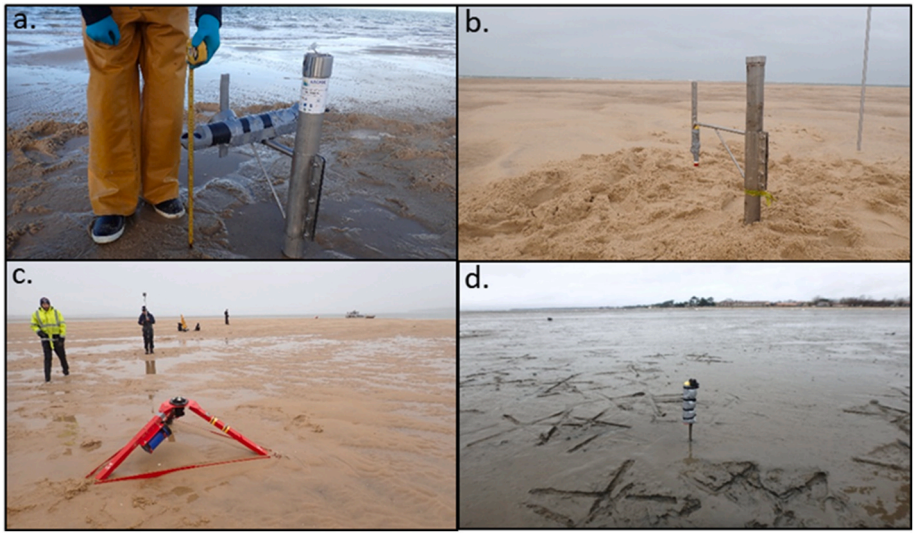

Fig. 2. Example of deployed Instruments, a. Aquadopp at location 112, b. RBR SoloD at location 114, c. ADCP S1000 at location 115, d. RBR Wave at location 18.

Table 1
Type of instruments and measurements used during the field campaigns.

ID	Sensor	Type of data	Acquisition	Frequency	Averaged water depth (m)
1	ADCP AWAC	Pressure/currents/free surface	burst	2 Hz	13.4
113	ADCP S1000	Pressure/currents/free surface	continuous	2 Hz	2.0
115	ADCP S1000	Pressure/currents	continuous	2 Hz	1.8
5	ADCP S500	Pressure/currents	continuous	2 Hz	5.7
112	Aquadopp	Pressure/currents	burst	2Hz/1Hz	1.4
4	ADCP Sentinel	Pressure/currents	burst	2 Hz	1.9
114	RBR soloD	Pressure	continuous	2 Hz	1.1
11	RBR soloD	Pressure	continuous	2 Hz	1.9
18	RBR Wave	Pressure	continuous	4 Hz	0.9

3.3. Data processing

The data processing is performed following the procedure detailed in Bertin et al. (2020). Bottom pressure measurements collected by each sensor were corrected for sea level atmospheric pressure measured at the local meteorological station of Cap Ferret (Fig. 1 a.) and time series were split into 30-min time windows. Free surface elevations were obtained from the hydrostatic reconstruction of the detrended relative pressure signal and then corrected using the linear transfer function (Kp, correction for non-hydrostatic effects, Svendsen, 2005) for point 1, 4, 5, 11, 115 and 18 and using the weakly dispersive method (Martins et al., 2021) for point 112, 113 and 114.

The variance density spectrum of the 30-min free surface elevation burst was computed with a fast-Fourier transform, using Hamming-window of 256 s with 50 % overlap (this gives 32.8 equivalent degrees of freedom, Priestley, 1981).

For observation data (Section 5.1), the total spectral significant wave height (H_{m0}) associated to the gravity and IG bands was calculated at

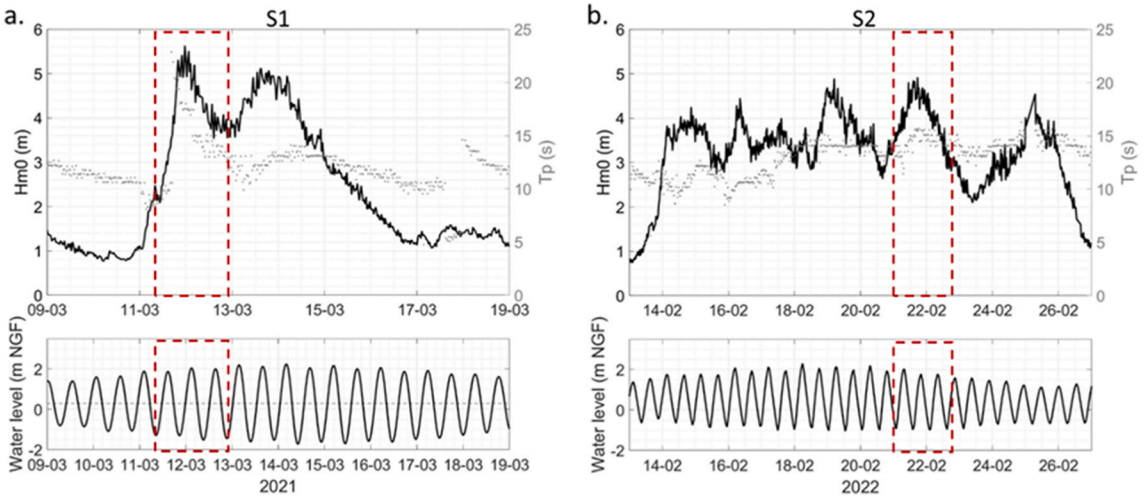

Fig. 3. Offshore storm wave time series at the Cap Ferret Buoy (observations for the 2021, 2022) and storm tide time series from the MARC operational model a) winter 2021 event and b) winter 2022 event. The red dashed rectangles bound the simulation periods for S1 and S2.

each location as:

$$H_{m0} = 4.\sqrt{\sum_{fmin}^{fmax} \mathrm{PSD(f).df}} \quad (1)$$

The frequency cutoff (f_{cut}) between SW and IG waves is time-varying and taken as $f_{cut} = f_p/2$ (Oh et al., 2020) with f_p is the offshore peak frequency (measured at Pt1) of a 30-min burst. SW contribution is computed between $f_{\min} = f_{cut}$ and $f_{\max} = 0.4$ Hz and IG waves contribution is computed between $f_{\min} = 0.004$ Hz and $f_{\max} = f_{cut}$.

In order to consistently compare observations and modeled wave characteristics, observations were also computed using a fixed $f_{cut} = 0.04$ Hz, and Root Mean Square wave Height (H_{rms}) obtained from the XBeach model were converted as follows:

$$H_{mo}, IG = \sqrt{2}.H_{rms}, IG \quad (2)$$

Comparison between observed and computed data were used to assess the model performance based on five parameters: water level; current velocity and direction; SW and IG waves height (noted $H_{m0,}SW$ and $H_{m0,}IG$ using classical statistical indicators (correlation coefficient R^2; Root Mean Square Difference, *RMSD*, and *Bias*).

4. Numerical modelling

4.1. XBeach model setup

4.1.1. Model description

To study the amplitude and spatial variability of IG waves in the Arcachon Lagoon during storms, the XBeach model (Roelvink et al., 2009) was implemented, based on the 2DH surfbeat solver (XB-SB; Roelvink et al., 2009; version 1.23 XBeachX release). XBeach is an open-source 2D depth averaged model, which solves for wave propagation, flow, sediment transport and bed-level changes for varying wave and flow boundary conditions. It solves the time-dependent short-wave action balance on the scale of wave groups, which allows for the reproduction of directional spread infragravity motions (so-called surfbeat) along with time-varying currents. The frequency domain is represented by a single representative frequency (spectral period $T_{m0\text{-}1}$). Shallow water momentum and mass balance equations are solved to compute surface elevation and flow. Additionally, to solve the contribution of short waves to mass fluxes and depth-integrated return flows, XBeach uses the Generalized Lagrangian Mean formulation (Roelvink et al., 2009). This model has been widely used to explore different questions related to IG waves in contrasting coastal environments. As reported by Bertin and Olabarrieta (2016), despite limitations due to the treatment of SW and IG waves in different models, XBeach is able to capture the main processes responsible for IG waves generation and propagation within inlet environments. For our study, calibration and performance of the model were realized against *in situ* observations located at the margin of the ebb delta within the inlet platform, the inlet shore and the internal part of the lagoon (Fig. 1 a. and b.).

4.1.2. Model implementation

The model has been implemented based on the recent topo-bathymetric survey DTM (Fig. 1 a.) by using a rectangular grid with variable cell size in both alongshore and cross-shore directions, covering a domain of approximately 33 × 33 km^2, with a spatial resolution ranging from 50 m to 10 m alongshore and 100 m–5 m cross-shore (the finer resolution being at the inlet), with a total of 1900 x 1 650 nodes. Bottom friction was represented by a quadratic bottom shear stress with a variable Manning coefficient, according to a 50 m-resolution Strickler map (Mugica et al., 2016), which resulted in a value of 0.019 at sea, 0.023 at the inlet and ranging from 0.03 to 0.05 in the lagoon depending on depth (secondary channels) and type of vegetation cover. These values are similar to Nahon et al. (2022), consistent with previous studies conducted on this site (Lavaud et al., 2020) and at other large-scale complex inlet system (e.g., Orescanin et al., 2016). The horizontal eddy viscosity was assumed to be constant (0.5 m^2 s^{-1}), and the minimum water depth was set to 0.02 m.

4.2. XBeach simulation

4.2.1. Sensitivity tests and model performance

In this study, two storm conditions (Fig. 3 a and b.) which occurred during the field campaigns were used for the parameter calibration procedure. Offshore wave conditions were extracted from the Cap Ferret Datawell WR buoy (anchored at 54 m depth). For simulations, 30 min-directional observed wave spectra were used as model forcing. Offshore tidal and atmospheric surge data have been collected from the MARC platform (Modelling and Analysis for Research in Coastal environment, www.umr-lops.org/marc), more precisely from the structured domain covering the whole Aquitanian coast with a spatial resolution of 250 m. The performance of the MARC modeling chains has been extensively validated at 19 tide gauges and 95 current meters in Pineau-Guillou (2013), and data are currently used for hourly runup and dune erosion predictions of the regional Aquitanian Early Warning System (Nicolae Lerma et al., 2018a, b).

A site-specific calibration is performed here to improve model skill, as in most applications of XBeach (Roelvink et al., 2018 and references therein). Model resolution was defined based on literature recommendations on minimum number of grid points per wavelength and a convergence analysis. A convergence analysis was performed using a 1D grid model, in order to evaluate the best compromise between the computational time and the model accuracy. This analysis revealed that a resolution of 5 m along the coast was satisfying, as a finer resolution did not significantly improve the results while dramatically increasing computational time. Due to the heavy computational time, the simulation of the storm events (S1 to S6, see Figs. 3 and 7) were performed only once (i.e., no ensemble). The use of random phase forcing (*random*) could introduce some variability from one simulation to another due to the random phase approach (e.g., Bertin et al., 2020), but it is argued that it does not impact notably the conclusions of this study. To verify this statement, shorter simulations made for the discussion section (section 6.2) were computed 2 × 5 times in order to overcome the random-phase issue and assess the relatively limited effect of the random phase forcing approach.

The two main parameters used for model calibration were identified through a literature review and sensitivity analysis: 1) the parameterization for depth-limited breaking, specifically the formulation of Roelvink (1993), called *roelvink2,* and the one from Daly et al. (2011); 2) the breaker index *gamma*.

An initial underestimation of IG waves was noticed at all sensors (including at the offshore location Pt 1, Fig. 1). This is usually attributed to the original surfbeat approach of XBeach, for broad directional shortwave spectra, where the wave energy from different directional bins is simply added up, and not considering the interference of the different wave components (Roelvink et al., 2018). In order to overcome this problem, the approach from Roelvink et al. (2018) is used, where the mean wave directions are calculated first and the SW energy is then propagated along these directions. Finally, the new method for the derivation of directional wave group energy propagation (*single-dir* option) that improves wave groupiness coherency is applied. This latter parameter allows for a better representation of IG waves, particularly under broad SW spectra. Table 2 lists the tested values.

Finally, the switch parameter (*wci*) for the wave-current interaction, was tested conducted during the calibration procedure and no significant differences in the results was observed (less than 5% in wave and current parameters). The reason for these low impact is that XBeach only accounts for the effect of the current on wave propagation (i.e., refraction and shoaling) and does not represent the dissipation by white-capping due to the increased wave steepness when short waves

Table 2
XBeach parameters considered in the model calibration. Italic are the default values, **Boldface** are the optimal values based on the calibration.

Sensitivity Parameters	Description	Values
Scheme	Second-order numerical scheme	***upwind_2***
Break	Type of breaker formulation	roelvink_daly and ***roelvink2***
gamma	Breaker parameter from Roelvink formulation	0.42, **0.47**, 0.52, *0.55*, 0.6
Single_dir	Turn on stationary model for refraction, surfbeat based on mean direction	**Active** or *not active*
wci	Feedback of the currents on the wave field	Active or ***not active***

propagate against currents. This limitation is mostly due to the single-frequency approach of XBeach while current-induced dissipation is frequency-dependent (e.g., Bertin and Olabarrieta, 2016; Mengual et al., 2022).

After calibration, the water level was well reproduced for the two events (Fig. 4), at the margin of the ebb delta (Pt 1), inside the inlet (Pt 5 and 115) and the lagoon (not shown), which confirms that tidal distortion is well captured by the model. We observe some mismatch at low tide for S2 (Fig. 4 d.) but without influence on the high tide water level fitting or on IG wave component (Fig. 5c., d.)

In terms of mean current velocity, the comparisons of observed and modeled data in the inlet are presented in Fig. 4 e and f. at Pt 5 and Pt 115 respectively. The RMSE are about 0.08 m/s (*U* component East) and 0.09 m/s (*V* component North) for S1 and 0.09 m/s (*U* component) and 0.12 m/s (*V* component) for S2, and R^2 is superior to 0.95 for all components, suggesting a very good representation of both current components.

At the margin of the ebb delta (Pt 1, Fig. 1), SW are fairly well reproduced (Fig. 5a and b), which is of primary importance to well-reproduce the IG waves amplitude above the ebb tidal delta. Considering the whole set of sensors deployed in the intertidal zone, wave heights were depth-limited and therefore strongly tidally-modulated. H_{mo},*IG* are reproduced by XBeach with a *RMSD* of 0.05 m, for S1, and 0.07 m for S2, corresponding to a *NRMSD* of 18% and 25%, respectively and systematically smaller than 20 % at the inner part of the inlet (Fig. 5 c. ,d. and Table 3). Those values correspond to good predictive skills compared to previously published studies which provided a detailed validation of XBeach based on extensive field *in situ* data (e.g., Bertin and Olabarrieta, 2016; Bertin et al., 2020; Mouragues et al., 2021; Nahon et al., 2023). These studies conducted to some extent in less challenging environments presents *NRMSD* typically ranging between 10 and 40%.

In addition to bulk parameters, time-averaged measured and modeled frequency distributions of the energy associated with IG waves during high tide are compared for several locations (at the ebb delta Pt 114, the inner part of the inlet (Pt 11, 115 and 4) and in the lagoon (Pt 5) in Fig. 6.

Although there is a mismatch in the peak energy intensity frequency at the ebb tide delta (Pt 114), the intensity and frequency of peak energies for Pt 11 and 4 are remarkably well simulated for the two event S1 and S2. This is clearly depicted for Pt 4, for which the double-peak shape of the spectra as well as the principal peak intensity (between 0.003 and 0.006 Hz) are well reproduced.

To summarize, XBeach model setup was calibrated using two energetic events, in 2021 and 2022 (Fig. 3 a., b.), and optimal parameters from the two best calibrations were similar. The values are reported in Table 2, and were used for all the other simulated storms (See the following Section). The simulations were computed over the entire duration of the storm (2–3 tidal cycles) and the time series of current velocities and surface elevations were used to compute and explore the waves characteristics.

4.2.2. Simulated scenarios

In addition to the two storms conditions (S1 and S2), four others storm conditions were simulated, corresponding to historical storms which occurred in 2009 (Klaus, S3), 2010 (Xynthia, S4), 2021 (Justine, S5), and an extreme statistical scenario S6 (see Fig. 7a., b., c., d. and Table 4). S3, S4 and S5 present contrasting forcing characteristics, in terms of water-level amplitude, offshore wave conditions and high tide/wave energy peak phase (see Table 3). Offshore simulation forcing (water level and bulk wave parameters) were extracted from the MARC platform and the Cap Ferret buoy at 10 min and hourly temporal resolution respectively (offshore bulk parametric wave characteristics).

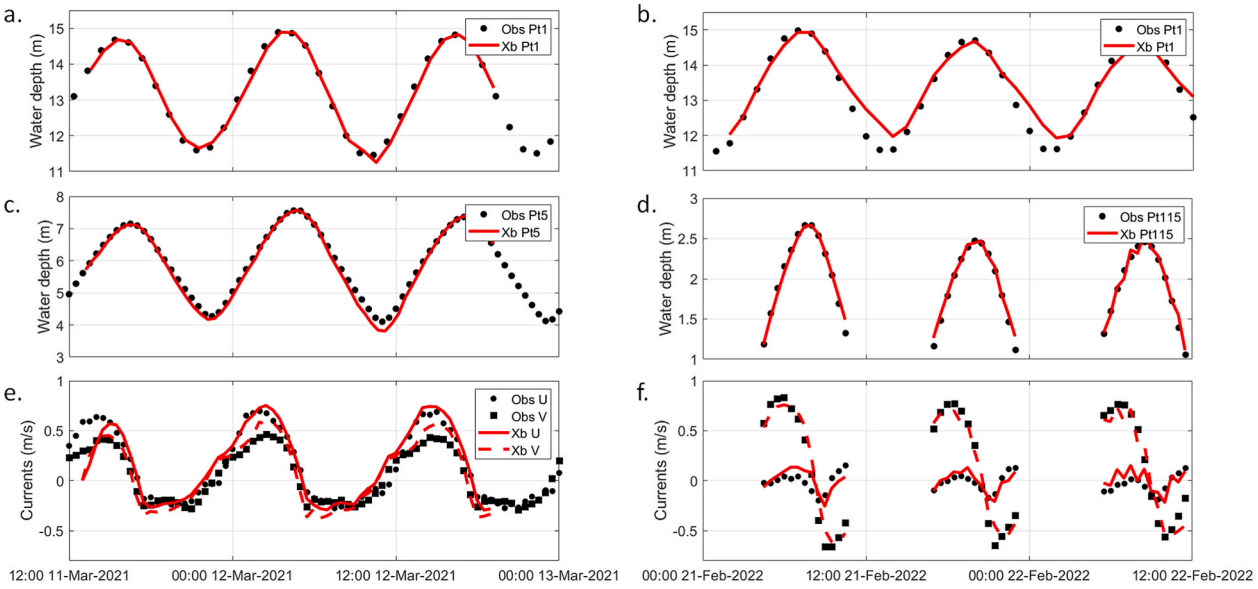

Fig. 4. Observed vs simulated water level and mean current velocity during S1 (left panel) and S2 (right panel), with a., d. the water levels at Pt1 (margin of the ebb delta), b., c. the water levels and e., f. the mean current velocities in the inlet at the location Pt5 and Pt115.

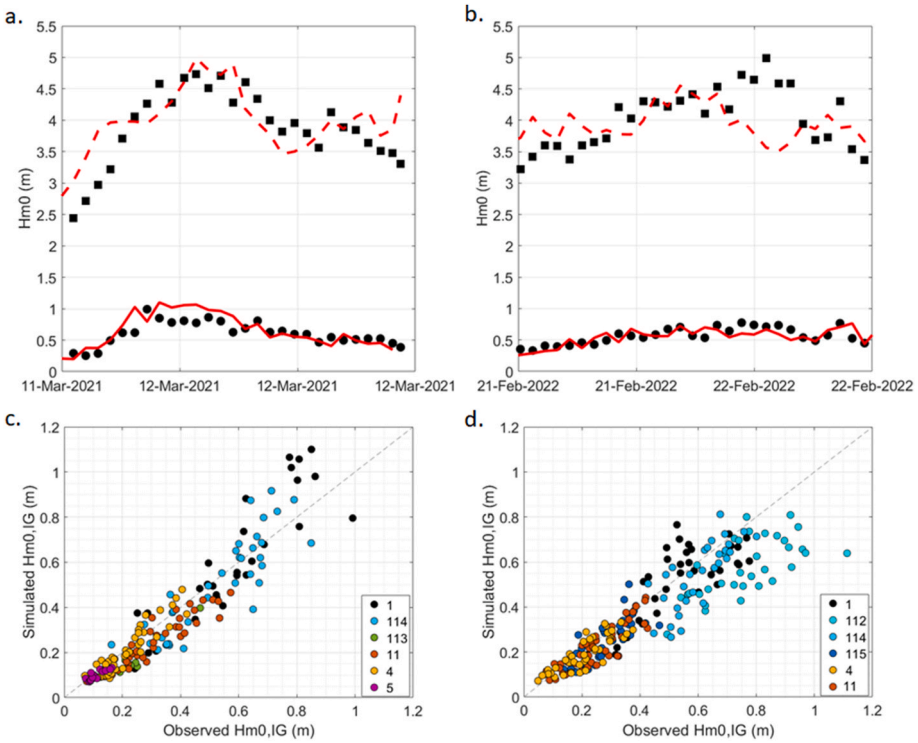

Fig. 5. Observed vs simulated wave parameters: Time series of observed (black symbols) and modeled (red lines) wave bulk parameters at the location of Pt 1 sensor (Fig. 1a), H_{mo},*SW* (black squares vs red dashed line) and H_{mo},*IG* (black circle vc red solid line) for the storms 2021 (a) and 2022 (b); (c–d) Observed vs Modeled H_{mo}, IG, with all sensors for the storms 2021 (c) and 2022 (d).

Table 3
Simulations vs observations statistics.

Storm	Sensor location	*Hrms* IG				*Hrms* SW			
		Bias(m)	R^2	*RMSD* (m)	*NRMSD* (%)	*Bias* (m)	R^2	*RMSD* (m)	*NRMSD* (%)
S1	1	0.02	0.83	0.11	0.17	0.13	0.77	0.35	0.18
	114	−0.02	0.86	0.07	0.13	0.24	0.87	0.27	0.39
	113	−0.05	0.84	0.06	0.25	0.13	0.55	0.23	0.36
	11	−0.05	0.91	0.06	0.09	0.17	0.78	0.25	0.32
	4	0	0.92	0.03	0.10	–	–	–	
	5	0	0.93	0.01	0.09	–	–	–	
	18	0	0.34	0.01	0.37	–	–	–	
S2	1	−0.02	0.68	0.09	0.28	−0.1	0.66	0.49	0.36
	112	−0.15	0.71	0.17	0.38	0.16	0.87	0.18	0.27
	114	−0.04	0.75	0.08	0.30	0.35	0.93	0.35	0.77
	11	0	0.78	0.05	0.18	0.39	0.68	0.44	0.63
	115	−0.02	0.79	0.05	0.20	–	–	–	
	4	0.01	0.83	0.04	0.15	–	–	–	
	18	0	0.65	0	0.29	–	–	–	

The storm S6 is an idealized scenario elaborated to simulate an extreme offshore storm conditions. Wave characteristics are based on the extreme statistic study from Bay of Biscay Wave Atlas eXtreme (BoBWAX; Nicolae Lerma et al., 2015) and are peaking at 100-year return value for the Cap Ferret buoy The offshore water level variation represents two tidal cycles reaching the spring tide water level at the study site during high tide. This forcing scenario, generated to simulate simultaneous maximum wave and water-level conditions, is used here to investigate the impact of an extreme wave event compared to common (observed) and historical storms.

5. Results

5.1. Observation of IG waves

For the two storm S1 and S2, Fig. 8 a., e. shows the offshore wave power and the tidal level over time. Fig. 8 b and f. show a decrease in H_{mo},*SW* between the edge of the ebb tidal delta platform (Pt 1) and the inlet (Pt 112 and 114), with values dropping from 4.5 to 1.5 m due to SW breaking over the ebb tidal delta. In contrast, the difference of H_{mo},*IG* between the edge of the ebb tidal delta and the inlet exhibits a more complex behavior. Fig. 8 c shows that during the peak of S1 at high tide, H_{mo},*IG* reaches values between 0.8 and 1 m at the edge of the ebb tidal delta (Pt 1), and between 0.7 and 0.9 m at the inlet (Pt 114). After the storm peak, H_{mo},*IG* does not exceed 0.6 m at Pt 1 while it reaches 0.7–0.8 m at the inlet. During S2 (Fig. 8 g.), H_{mo},*IG* increases over the

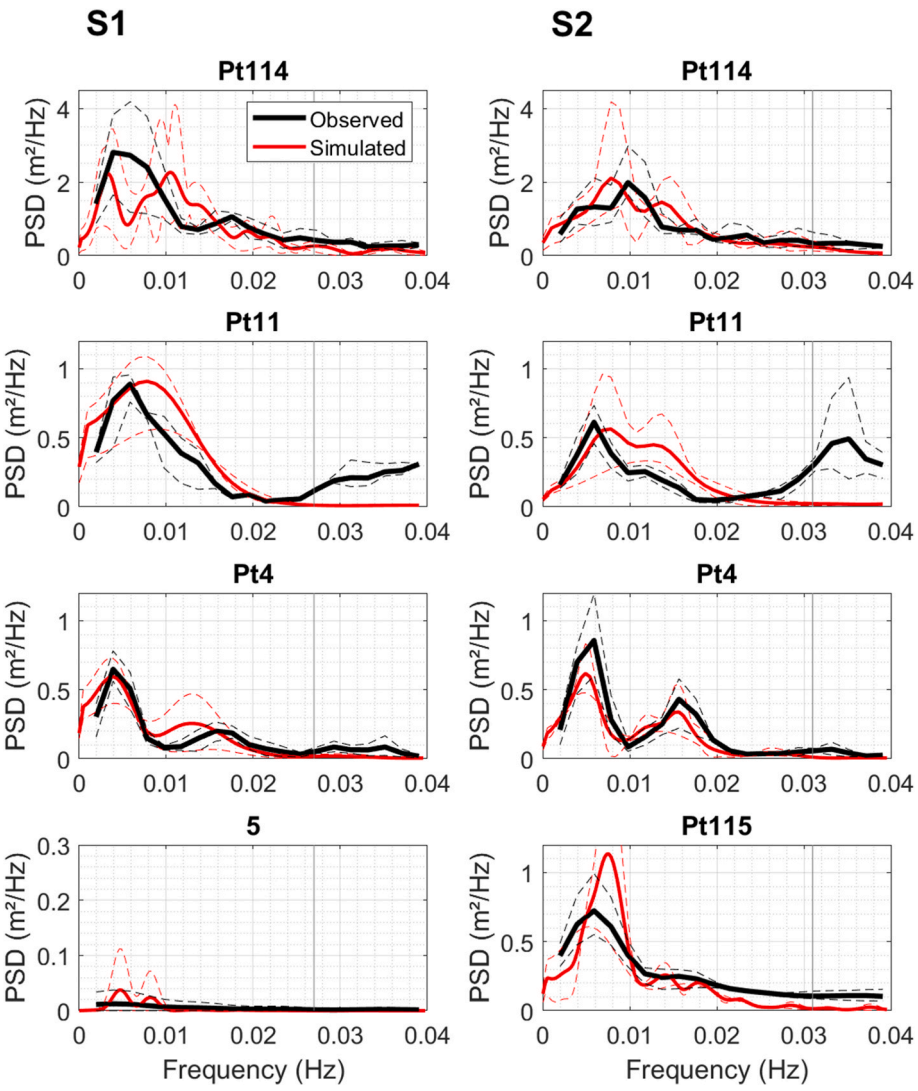

Fig. 6. IG wave energy density spectra at the internal part of the inlet at high tide during the S1 (left panel) and S2 event (right panel). Observed and simulated time-averaged spectra during high tide (2 h) are depicted in black and red solid line, respectively. Dashed lines represent the 95% confidence interval. The vertical grey line indicates the fcut = 0.5*(1/*Tp*).

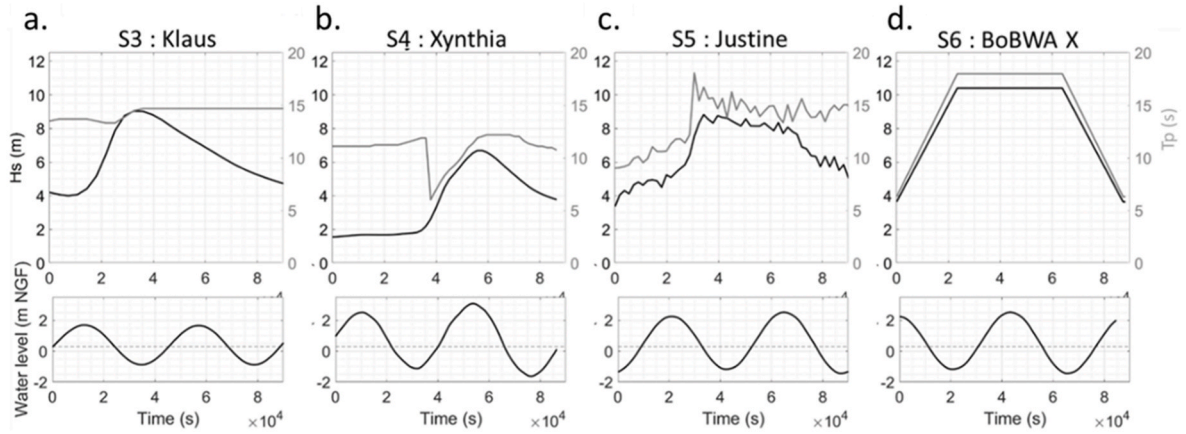

Fig. 7. Offshore storm wave at the Cap Ferret Buoy and storm tide time series for historical and idealized storms. Subplots a), b), show the forcing conditions for historical storm (data extracted from the MARC operational model platform at the Cap Ferret buoy location), with S3 (Klaus event, simulation time from January 23, 2009 21h00) and S4 (Xynthia event, simulation time from February 27, 2010 14h00). Subplot c) Illustrate the observed condition at Cap Ferret buoy location for S5 (Justine event, simulation time from January 30, 2021 13h00 and d) represents the extreme idealized storm.

Table 4
Characteristics of the simulated storm events (WP value during the wave peak conditions, EP value of waves during the water elevation peak, at Pt1)).

Storm	Type of storm	Date	Wave event return period	Moment of the storm	Maximum water level (m *NGF*)	Maximum H_m0 or H_s in (m)	Maximum T_p (s)	Maximum D_p (°N)
S1	Observed	March 2021	>Annual	WP	0.7	5.6	17.5	281
				EP	2.1	4.7	15	283
S2	Observed	February 2022	>Annual	WP	1.1	4.9	15.6	288
				EP	2	4.3	13.1	290
S3 (Klaus)	Historical	January 2009	10–20 year	WP	−0.6	9.03	14.5	277
				EP	1.63	7.1	14.7	276
S4 (Xynthia)	Historical	February 2010	≈1 year return period	WP	2.8	6.7	12.2	266
				EP	3.1	6.5	11.4	264
S5 (Justine)	Historical	January 2021	≈10-year return period	WP	−0.3	8.8	16.7	275.5
				EP	2.5	8.3	14.4	275.6
S6 (BoBWAX)	Statistical	–	100 y return period	WP	2.2	10.4	18	270
				EP	2.2	10.4	18	270

platform from 0.8 m at Pt 1 to more than 1 m at Pt 112. It was observed that variations in the offshore power and tidal water level yield to variations in the location of the first bathymetry-induced breaking, explaining why IG waves at the inlet (Pt 114 and 112) can be similar, lower or even higher than offshore (Pt 1) under different conditions (Bayle et al., 2022).

At the inner part of the inlet (Pt 11, 4, 115), the observed values of H_{mo},*IG* during the two events S1 and S2 are quite similar (Fig. 8 c and g.). In the inner part of the inlet directly exposed to offshore waves (Pt 11), H_{mo},*SW* is about 1–1.5 m and H_{mo},*IG* are similar about 0.4–0.6 m for the three locations (Pt 11, 4, 115). At the entrance of the lagoon (Pt 5), H_{mo},*IG* are still substantial and reach about 0.1–0.2 m (Fig. 8 c.), while along the eastern shore of the lagoon (Pt 18), H_{mo},*IG* is residual, about a few centimeters. Inside the lagoon, H_{mo},*SW* coming from the inlet are residual and the H_{mo},*SW* wave spectra show that offshore wave are dissipated and SW are only generated by the local wind reaching 0.1–0.2 m (Bayle et al., 2022).

Fig. 8 d and h., show the ratio between H_{mo},*IG*/H_{mo},*SW*. At the edge of the ebb tidal delta (Pt 1), this ratio is small and ranges from 0.1 for low-energy to 0.2 for high-energy offshore wave conditions, without any clear tidal modulation.

Interestingly during high tide, the ratio H_{mo},*IG*/H_{mo},*SW* (Fig. 8 d and h.) at the inlet shore (Pt 11 and Pt 4) shows that IG waves dominate the variance of the free surface elevation during storm events. At the more exposed coast (Pt 11), this ratio peaks between 1 and 1.5, similar to the values observed at the flood tidal delta (Pt 115). In the sheltered part of the inlet (Pt 4), the ratio ranges between 1 and 2 at high tide, and reaches 2.5 at the beginning of the ebb (during S2). Over a tidal cycle, an asymmetric pattern is clearly visible, with values usually higher at mid-ebb than mid-flood. This pattern, similar to the one showed in Bertin and Olabarrieta (2016), is particularly clear during S2 at Pt 4, Pt 11 and Pt 115 with a ratio H_{mo},*IG*/H_{mo},*SW* two times larger at mid-ebb compared to mid-flood.

For the two observed events S1 and S2, field measurements showed that significant IG waves were observed during common winter storms in the inlet and lagoon. However, the spatial coverage of the field campaign was limited and the instrument locations were often away from the shore. Therefore, the use of a model is required to better understand the processes controlling IG waves propagation and evaluate their contribution to TWL.

5.2. Simulating IG waves

5.2.1. During common storms

The XBeach model was used with the first objective to complement the observations of IG waves within the inlet during storms, and investigate the spatial variability of IG waves along the inlet, particularly the alongshore variability at the coast. The maximum value of H_{m0},*IG* of the simulated storm time series (hereafter referred to as 'IG_{max}') was extracted along the coast at the last always-wet cell.

H_{m0},IG_{max} simulated along the shore of the inlet, gradually decreases towards the lagoon (Fig. 9). The values along the open beaches (B1 and B11) at the edge of the inlet range between 0.85 and 1.85 m, with longshore average value of 1.15–1.40 m. At the Cap Ferret spit (B2-B4), the alongshore average value is 0.87 m at the area B2 and progressively decreases, but remains important in the sheltered part with a value of 0.59 m and 0.25 m at B3 and B4, respectively. At B3, at the proximal end of the Mimbeau Spit (near Pt 4, Fig. 1 a.), H_{m0},IG_{max} locally reaches 0.80 m–1 m. These simulation results are consistent with *in situ* observations and are discussed in Section 6.

At the Eastern part of the inlet (B5 – B10), B5 presents similar value as B4 with H_{m0},IG_{max} around 0.3 m, which are representative values of the entrance of the lagoon. From B6 to B8, H_{m0},IG_{max} shows weak spatial variability with an average of 0.55 m. At B9, which is located in the shadow of the largest sand bank (Banc d'Arguin) of the inlet, H_{m0},IG_{max} drops to 0.3 m on average, but drastically increases further south at B10

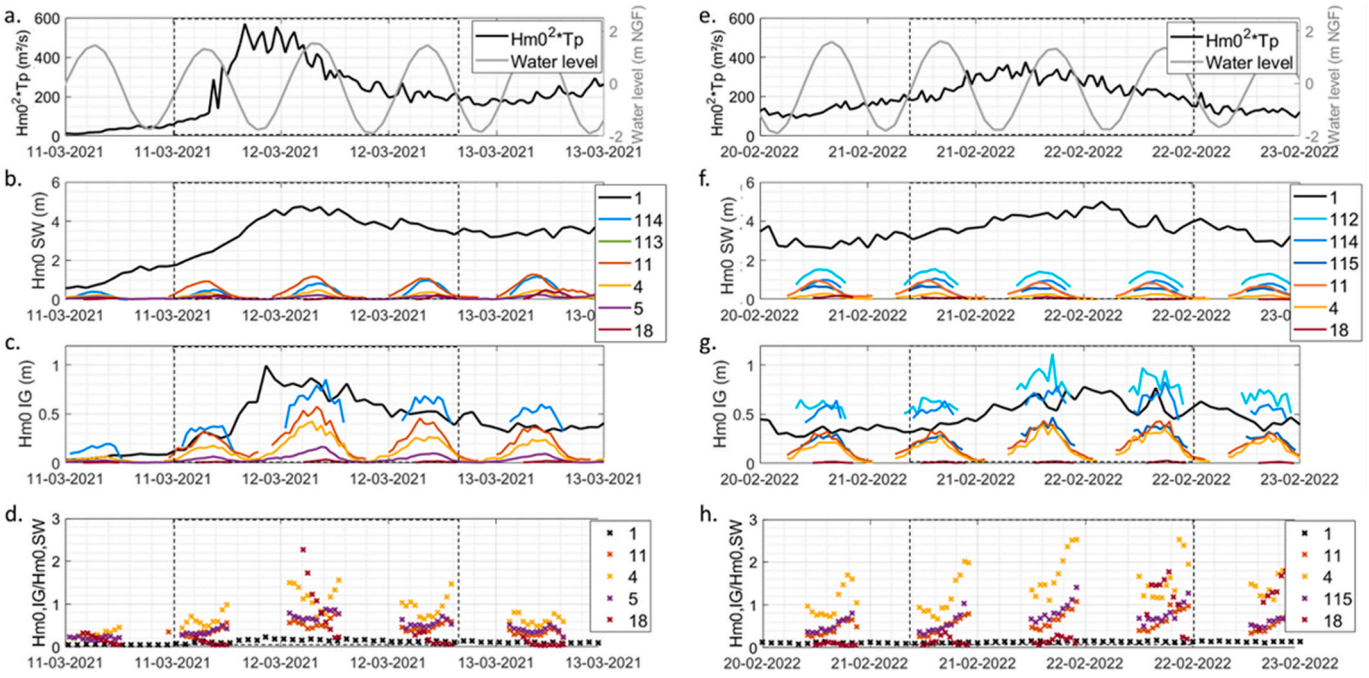

Fig. 8. Offshore wave power and water-level conditions during the storm S1 (a.) and S2 (e.), SW (b., f.), IG waves height (c., g.) and H_{mo},IG/H_{mo},SW ratio (d., h.) for S1 and S2 respectively. Color points are from the margin of the ebb delta to inside the lagoon (see Fig. 1 for location). The dashed box indicate S1 and S2.

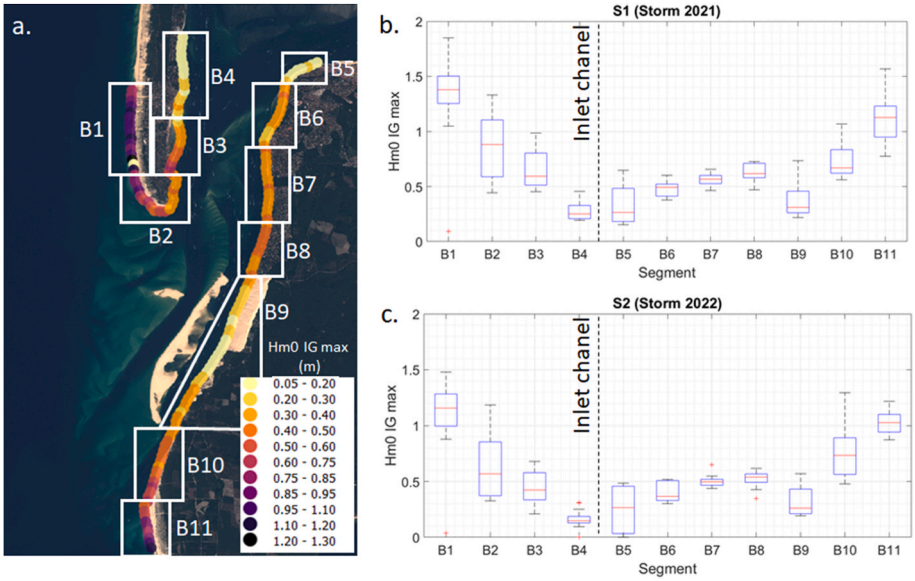

Fig. 9. Simulated IG wave significant wave height peak (H_{m0},IG_{max}) at the coast, a) during the storm S1 (2021) and delimitation of coastal segment, b) and c) box plot for the delimited coastal segment for S1 and S2 respectively. On each box, the central mark indicates the median, and the bottom and top edges of the box indicate the 25th and 75th percentiles, respectively. The whiskers extend to the most extreme data points not considered outliers, and the outliers are plotted individually using the red '+' marker symbol.

with 0.66 m on average and locally up to 0.85 m. The simulated H_{m0}, IG_{max} at the inlet coastlines are in agreement with the observations (Pt 11 and Pt 4), confirming that IG waves can play an important role all along the inlet shore.

5.2.2. *During historical and extreme storms*

The second objective of using the XBeach model was to analyze the contribution of the IG waves to the TWL along the coast for historical storms as well as for an idealized extreme wave event (Fig. 3).

Fig. 8 a and b. show H_{m0},IG_{max} along a transect from the ebb tidal delta, through the flood tidal delta, to the lagoon. At the edge of the ebb tidal delta (Fig. 8 a.), at a comparable depth and exposure as Pt 1 (≈15 m depth), H_{m0},IG_{max} shows remarkable variability depending on the simulated storm (between 0.5 and 1.4 m). From the margin of the ebb tidal delta, H_{m0},IG_{max} value rapidly increases, peaking at the inside edge of the ebb tidal delta as depth decreases. Note that the more energetic the offshore wave conditions, the further offshore H_{m0s},IG_{max} peak is located. After the peak, which reaches 1.60 m for the extreme scenario

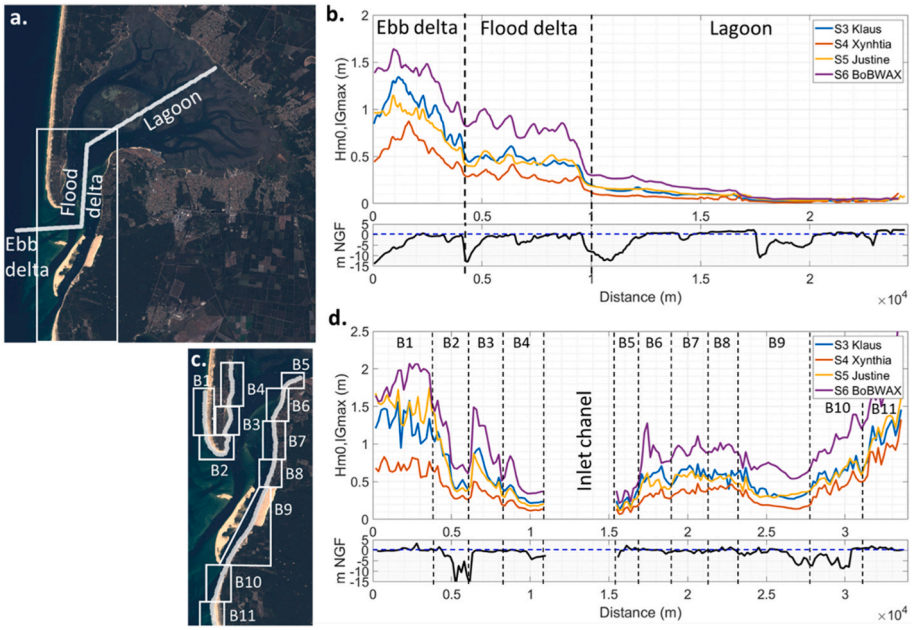

Fig. 10. Simulated IG wave significant wave height peak along the inlet at the coast for historical and extreme storm conditions: a) location of cross inlet-lagoon transect b) H_{m0},IG_{max} and bathymetry profile, c) delimitation of coastal segment at the inlet, d) H_{m0},IG_{max} at the inlet coast.

S6, H_{m0},IG_{max} progressively decreases over shallow water depth, with local increases and decreases likely due to bathymetric variations. IG waves decay across the surf zone was observed in several studies (Ruju et al., 2012; Mendes et al., 2018; Rijnsdorp et al., 2022) but to date, the underlying reasons remain unclear and are beyond the scope of this work. In the inner part of the inlet, over the flood tidal delta, H_{m0},IG_{max} ranges from 0.3 m to 0.85 m depending on the storm conditions and slowly decreases over this shallow area. When entering the lagoon, H_{m0}, IG_{max} drops dramatically below 0.3 m for all storm cases. It continues to decrease on the shallow muddy and seagrass platform but remains non-neglectable until the center of the lagoon. Finally, H_{m0},IG_{max} are residual along the shoreline of the inner part of the lagoon (as measured at Pt 18).

Along the shore of the inlet, (Fig. 10c., d.) following the same delimitation as proposed in Fig. 9, H_{m0},IG_{max} are related to offshore wave conditions with values around 0.4 m for S4, between 0.55 and 1 m for S3 and S5 and reaching 0.85–1.5 m for S6 (Fig. 9d.). Simulations also confirm no notable differences on both side of the inlet, between B3-B4 (sheltered coast) compared to B5-B8 (exposed coast). Locally, a clear increase in H_{m0},IG_{max} is observed in B3, and local peak is observed in B6 for S6 only. The reason for this local amplification is hypothesized to be related to IG wave reflection within the inlet and local resonance, and is discussed further in Section 6.

The simulated H_{m0},IG_{max} along the inlet coast for the historical storms (Klaus, Xynthia, Justine, Fig. 8d.) are quite comparable to the storms S1 and S2 (Fig. 6c., g.). Although H_{m0},IG_{max} values reached during the extreme storm scenario (S6) are notably higher (around 1 m), they do not increase linearly with offshore wave power.

5.3. IG waves VS offshore wave power

Fig. 11 shows observed and simulated H_{mo},IG versus the offshore wave power ($H_{m0}^2.T_p$) at high tide for different locations in the inlet. For simulated events, the values considered are the longshore average value of the sector (sector B3 and B8 for sheltered and exposed coast, respectively) and do not underline local amplifications as observed in Fig. 10d. The local value of H_{mo},IG (in the inside part of the ebb tidal delta Pt 114, the inlet wave-exposed Pt 11 and wave-sheltered coast Pt 4) depends firstly on the offshore wave power. The tidal water level was

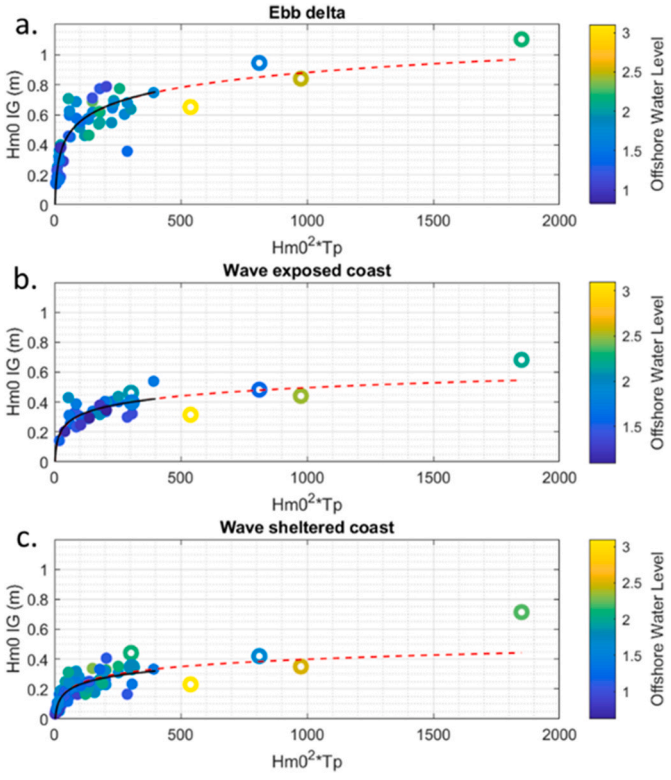

Fig. 11. H_{mo},IG vs offshore wave power at high tide a) at the inside part of the ebb tidal delta platform (Pt 114), b) at the wave-exposed coast (Pt 11), c) at the wave-sheltered coast (Pt 4). Filled circles are observations, unfilled are mean value derived from the simulations. The black line is the logarithmic adjustment based on observations, the red dashed line the extension considering simulations of historical and idealized storms.

expected to have an effect on H_{mo},IG, with larger IG waves at high tide due to possibly larger reflection over usually steeper beach upper part. Yet, the observations as well as the simulations reveal a scattered

behavior, suggesting that tidal variations (neap or spring tide) and also atmospheric surges do not have a significant effect on H_{mo},IG at the inlet shore (Fig. 11).

As expected, H_{mo},IG is maximal at the ebb delta (Fig. 11a.), but surprisingly, the values (observations and simulations) are similar at the wave-exposed (Pt 11-B8) and wave-sheltered coast of the inlet (Pt 4-B3), Fig. 11b., c. In addition, even if offshore wave power can be more than three times higher, IG waves within the inlet are quite comparable for the three areas. The logarithmic adjustment of the fitting line based on offshore wave power (red line in Fig. 11a., b. and c.) is statistically significant with $R^2 = 0.85$; 0.56; 0.74 for the platform, the wave exposed and sheltered coast respectively. This highlights that, at least for the internal part of the inlet, the alongshore averaged H_{mo},IG reaches a threshold value around 0.4 m–0.6 m for offshore energy levels $H_{m0}^2.T_p >$ 200–250 m^2 s.

6. Discussion

6.1. IG waves within the inlet

In previous studies, the propagation of IG waves has been found to be substantial in small small-scale inlets (Bertin and Olabarrieta, 2016). As it is observed at the inner part of the inlet (Fig. 8, Pt11, 4, 115), Bertin and Olabarrieta (2016), found that IG waves reach their maximum at high tide and brutally decrease since the beginning of the ebb due to tidal counter current effect on propagating waves. Note that Bertin and Olabarrieta (2016) and Bertin et al. (2019) also showed that IG wave blocking could occur in the end of the ebb in shallow inlets. Nevertheless, this process can only occur under strong opposing currents in very shallow depth (i.e. < 1m), which conditions can only be met very locally (i.e. some regions of the ebb delta) in a large inlet such as Arcachon.

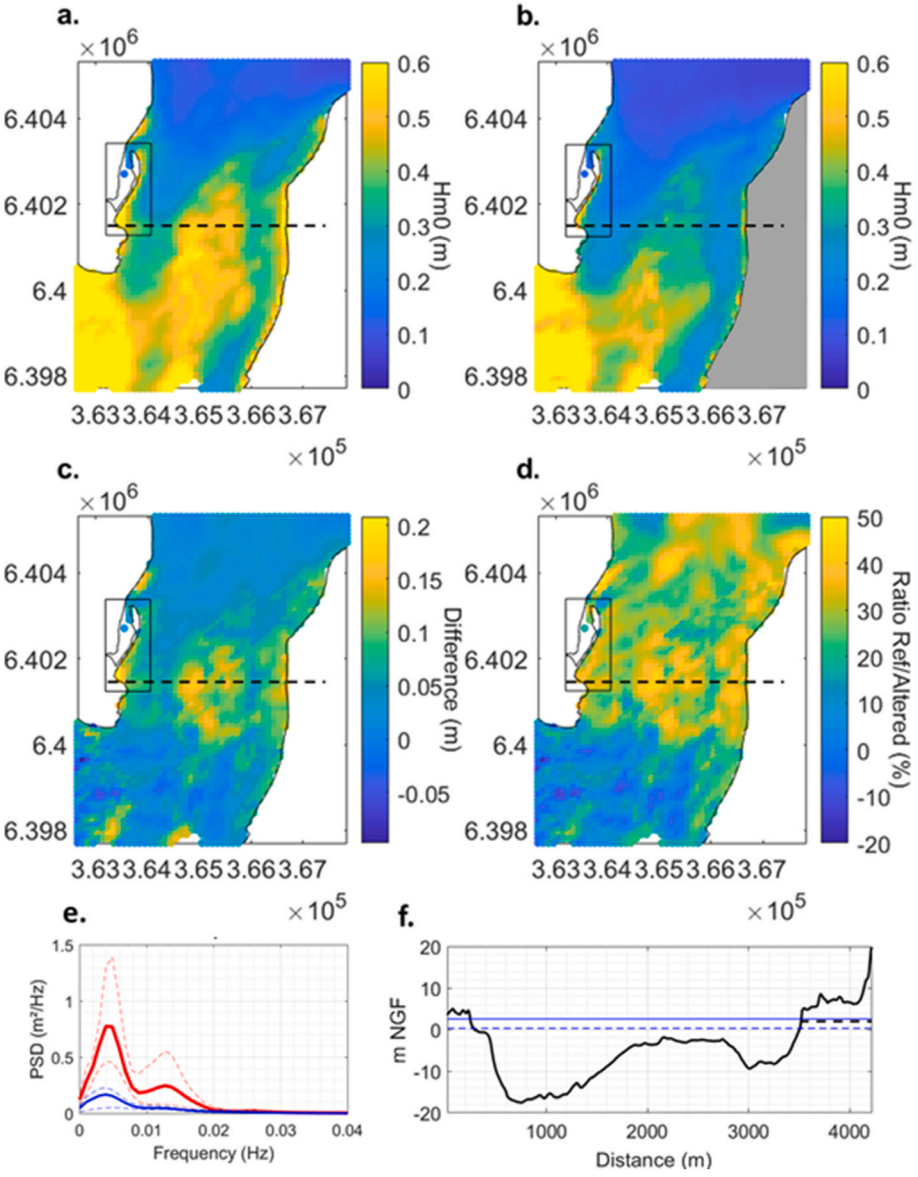

Fig. 12. H_{m0},IG_{max} at internal part of the inlet for S1 storm with a.) the reference bathymetry, b.) the altered bathymetry (modification of the wave-exposed coast topo-bathymetry (the grey area), c.) H_{m0},IG_{max} difference, d.) ratio between the difference and the original simulation, e. IG wave energy density spectra at the proximal end (Pt 4 locations) of the Mimbeau Spit (black rectangle). The red and the blue curves represent the time-averaged spectra during high tide (2 h) on the reference and the altered bathymetry, respectively. Dashed lines represent the 95% confidence interval. f.) illustrate the topo-bathymetric cross-channel profile (along the dashed line in a., b., c., d. subplot), black solid and dashed lines illustrate the reference and the altered topo-bathymetry, respectively. The blue solid and dashed lines, high tide water level (2.5 m *NGF*) and the mean sea level, respectively.

During a storm with comparable offshore wave conditions as S1 and S2 ($H_s \approx 5$ m and $T_p \approx 13$–16 s), Mendes et al. (2020) observed IG waves values of $H_{m0} = 1$ m along the adjacent shoreline of a small inlet and up to 0.4 m inside the lagoon. Our observations are similar with H_m0, *IG* between 0.8 and 1.1 m at the ebb delta platform and between 0.3 m and 0.7 m along the shores of the inlet demonstrating that IG wave play an important role at large scale inlets, including at the internal part and suggest that independent to specific size or morphology, IG wave in such environment depends mainly on offshore forcing conditions, including the width of the incident wave spectrum (Bertin et al., 2020). However, based on observations and simulations, it was shown that some parts of the inlet coast are submitted to local amplification of H_{mo},*IG* (Fig. 10d) with the main example is observed at the proximal end of the Mimbeau Spit (B3). In order to explore the process related to this local amplification, two analyses are proposed.

First, a numerical experiment was performed (Fig. 12) to quantify the possible contribution of IG wave reflection within the inlet. To this end, we compared the original H_{m0},*IG* results of the S1 simulation (Fig. 12a.) to a simulation with the same offshore forcing but with a modified topo-bathymetric model (Fig. 12b.). The new topo-bathymetric model (called altered bathymetry) has been modified to present a flat platform above 2 m *NGF* at the wave-exposed part of the inlet. The platform extends over several kilometers to allow the progressive dissipation of IG waves and avoid reflection. In this configuration, we consider that at high tide (water level above 2.5 m *NGF*), the major part of the IG waves coming from offshore are decaying on the flat area and do not reflect.

Considering that H_{m0},IG_{max} is reached at high tide, the results show that the difference in H_{m0},IG_{max} between the two bathymetric configurations is substantial (from 0.1 to 0.25 m) at the shore of the inlet and above the flood tidal delta (Fig. 12c.). Fig. 12d shows the percentage of the total signal explained by the reflection at the wave exposed coast of the inlet: a great part of H_{m0},IG_{max} is due to IG wave reflection from one coast to another (reaching more than 50 % within the inlet). It is particularly the case for the sheltered part of the inlet, at the proximal end of the Mimbeau spit and further North were H_{m0},IG_{max} locally drops by 35–40 % if IG waves reflection along the eastern side of the inlet is disabled through the modification of the bathymetry (see Fig. 12e.).

The second reason investigated to explain this amplification is linked to the local morphology of the coastline. The simple analytical model of Rabinovich (2009) for a semi-enclosed basin has been applied to the little bay at the proximal end of the Mimbeau spit, to determine the period T_0 of the fundamental mode:

$$T_0 = \frac{4.L}{\sqrt{g.h0}}$$

Where *h0* is the mean water depth, *L* is the mean length of the bay and *g* is the acceleration of the gravity (9.81 m s^2). Considering a mean water depth *h0* = 3 m–4 m at high tide and a mean basin length of 400 m (Fig. 12f.), the fundamental mode of the Mimbeau Bay at high tide has a period of ~250–300 s, which matches the range of periods amplified (see Figs. 6 and 12e.).

To summarize, most of the waves feeding the resonance at the sheltered shore are the result of reflection from one coast to the other. However, the significant part of the energy present in the spectrum obtained with the altered bathymetry (i.e. reduced reflection) suggests that a non-negligible part comes from the propagation of IG waves along the Cap Ferret coast. However, the numerical simulation with the altered bathymetry cannot guarantee a total eradication of the reflection process, and therefore the origin of the residual signal requires further investigation. Following the same reasoning, the local peaks in B4 and B6 (see Fig. 10) are hypothesized to be caused by the same processes (multiple reflection from one coast to the other and local amplification). These results also suggest that this kind of amplification should be observed in similar environments (large inlets and estuary mouth), depending on the topo-bathymetric configuration.

6.2. IG wave contribution to TWL

The contribution of IG waves to the Total Water Level (TWL) is particularly significant along wave-exposed beaches (e.g., Nicolae Lerma et al., 2015; Baumann et al., 2017; Bertin et al., 2018; Gallien et al., 2018; Fiedler et al., 2018; Nahon et al., 2023), but to date, their contribution along the shores of large inlets remains poorly understood and has not been studied. In the context of early warning systems dealing with both submersion issues and hazard mapping, the lack of an estimate of the impact of IG waves during storms is a major shortcoming.

There is no ideal way to evaluate IG waves-induced swash (S_{IG}) from H_{mo},*IG* in such environment. On the one hand, numerical models require high spatial resolution (O(1 m)) in order to accurately estimate the swash (Stockdon et al., 2014, Nicolae Lerma et al., 2015), which was not achievable in this large scale studies. On the other hand, empirical runup formula have generally been adjusted on observations made on beaches directly exposed to waves (Stockdon et al., 2006). Nonetheless, some studies on dissipative to highly dissipative beaches (Guza and Thornton, 1982; Ruessink et al., 1998; Ruggiero et al., 2001) have demonstrated that the influence of SW on the swash can be neglected, and proposed several empirical formula to estimate the IG-wave induced swash. As a first estimation, and because it has been observed that IG waves dominate the forcing at the shore of the inlet during storms, several formula proposed in the literature were compared (Guza and Thornton, 1982; Ruessink et al., 1998; Ruggiero et al., 2004, noted Gu82, Rue98, Rug04 respectively), to estimate the S_{IG} contribution to the TWL.

Fig. 13a and b. show S_{IG} for the common storm conditions (S1) and for an extreme storm (S6). We observe that the Gu82 and Rug04 formula propose relatively homogenous estimation on both sides of the inlet (B3, B6, B7 and B8) with values (25th and 75th percentiles) between 0.4 and 0.6 m for S1 and 0.6–0.9 m for S6. The more exposed segment to high S_{IG} is B3, in the sheltered part of the inlet with value peaking at 0.74 m for a common storm, and 1.1 m for an extreme storm (Gu82 formulation). Estimation proposed by the Rue98 are consistently lower mostly because the constant of proportionality in the linear fit relating S_{IG} and H_s (H_{m0}) is smaller, which was attributed to lower offshore wave period condition in their original dataset (Ruggiero et al., 2004). Note that these formula do not differentiate between incident and reflected components in the forcing (H_{m0}) which can lead to an overestimation of the value of S_{IG}.

Fig. 13c illustrates the logarithmic regression fitted on S_{IG} calculated using the Guza82 estimator ($R^2 = 0.74$) thanks to H_{mo},*IG* observations at Pt 11 and Pt4 and alongshore-average simulated values for B3 and B8. Fig. 13d show observations and simulations as they have shown similar H_{mo},*IG*, S_{IG} at the inner part of the inlet (corresponding to B3, B6, B7 et B8 sectors) can reasonably be estimated with the same expression as:

$$S_{IG,Gu82} = 0.079 \log(H_{m0}^2.T_p) - 0.121$$

This expression allow estimating more realistic values for weak waves conditions than other tested (i.e. Rug04, grey curve in Fig. 13c but note that the estimated values of S_{IG} for H_{mo},*IG* > 0.4 m are equivalent with to those proposed by the formula of Rug04. It is suggested to use the Gu82 regression for offshore wave conditions with $H_{m0}^2.T_p < 1\ 000$. Further research (observation and simulation) needs to be done for extreme energetic events (particularly for storms characterized by very large peak period, i.e., $T_p > 18$ s) in order to confirm the representativeness of the S6 results.

6.3. Relative contribution of wave-induced process to TWL

Several studies have shown the notable contribution of the wave-induced setup (noted η) to TWL at estuary mouth, inlets and connected semi-enclosed lagoons (e.g. Hanslow et al., 1996; Bertin et al., 2009; Malhadas et al., 2009; Dodet et al., 2013, Fortunato et al., 2021; Wargula et al., 2014, Lavaud et al., 2020). These studies demonstrated that η, (i) can contribute of tens to several tens of centimeters on

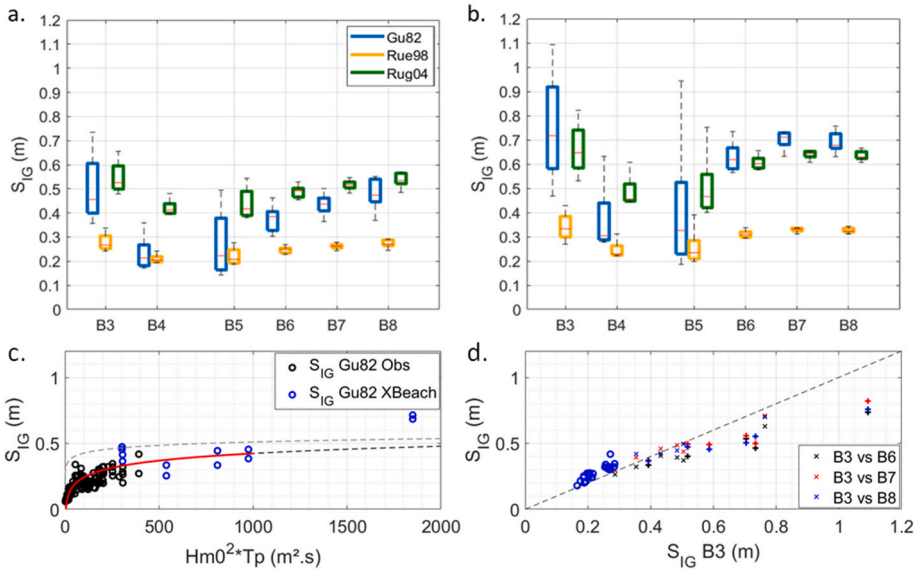

Fig. 13. Wave induced swash (S_{IG}) estimates for a.) S1 (common winter storm) and b.) S6 (statistical extreme storm) with the formulation: $S_{IG} = 0.71H_{mo} + 0.035$ (Guza and Thornton, 1982, noted Gu82); $S_{IG} = 0.18H_{mo} + 0.16$ (Ruessink et al., 1998); $S_{IG} = 0.33H_{mo} + 0.33$ (Ruggiero et al., 2004, noted Rug04) along the coast of the inlet, (refer to Fig. 9 for the delimitation of the coastal segment). The subplot c.) Illustrates the relation between the offshore wave energy $H_{mo}^2.Tp$ and the S_{IG} based on the Gu82 estimator. Circles represents observations at Pt11 and Pt4 (dark) and alongshore-average simulated (blue) values for B3 and B8. The red solid curve prolonged by the black dashed line is the log regression associated to the Gu82 estimator for alongshore-averaged S_{IG}. The grey curve is the log regression associated to the Ru4 estimator. The subplot d.) illustrates the relation between S_{IG} at wave exposed shore of the inlet (B6, B7, B8) with respect to the sheltered part of the inlet (B3). Circles, thin (x) and bold (+) crosses represent observations, alongshore-averaged and alongshore-maximum values respectively.

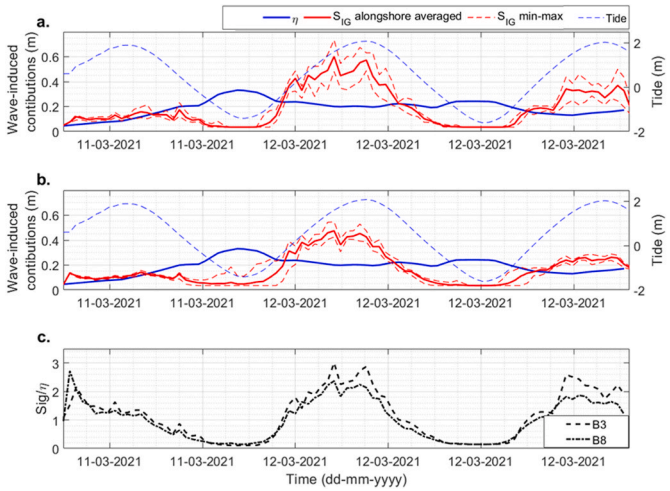

Fig. 14. Time varying *SW*-induced setup (η), alongshore average IG-induced swash (S_{IG},Gu82) and Tide at the internal part of the inlet for the S1 event, a.) along B3 and b.) along B8 coastal segment. The subplot c.) represents the S_{IG}/η ratio for the two coastal segment.

quasi-static water level, (ii) extend at the scale of the whole lagoon, (iii) reaches maximum values in anti-phased with tidal water level (i.e., is maximum at low tide). As a consequence, the wave setup contribution to TWL has been considered as an essential process to characterize and evaluate flood hazard in such environment (e.g., Hanslow et al., 1996; Lavaud et al., 2020). In comparison, to the authors' knowledge, the relative contribution of IG waves to TWL has not been evaluated at inlet shores. The contribution of η has been computed using the stationary solver of XBeach applied to storm S1 conditions, and has been compared with alongshore-averaged and min-max $S_{IG,Gu82}$ at the internal (B3) and exposed (B8) part of the inlet (Fig. 14).

The contribution of η reach 0.33 m and 0.2 m at the low tide and high tide peak respectively and with very similar values at the inlet and in the lagoon. These values correspond to 5 % to 7% of the offshore significant wave height, which is a comparable ratio to the one obtained by Lavaud et al. (2020) during the Klaus storm at this study site, but lower than the ratio obtained in shallower inlets (Dodet et al., 2013). In comparison, $S_{IG,Gu82}$ is in phase with the tidal elevation and reaches in average between 0.4 m and 0.6 m on the both sides of the inlet. Therefore, considering the ratio $S_{IG,Gu82}/\eta$, $S_{IG,Gu82}$ is 2–3 times larger than η at high tide when the flood potential is maximum. In conclusion, using modelling tools that ignore IG waves processes (that can lead to rapid water level increase) are rather incomplete and very likely prone to under-estimate the absolute TWL and associated risk for coastal flooding. Future work in modelling and early warning system should focus on the implementation of these forcings.

7. Conclusion

The combination of *in situ* hydrodynamic measurements at several locations of the large Arcachon inlet-lagoon system during winter storms and successfull modeling (XBeach model) over a wide computational domain encompassing storms of varying intensity, has revealed a substantial contribution of IG waves to the variance of free surface elevation during storms. Their contribution, through IG wave-induced swash, to the Total Water Level (TWL) at the shore on both sides of the inlet and at the entrance of the lagoon is related to offshore wave conditions. It exceeds by a factor of 2–3 the contribution of wave-induced setup and potentially play a major role in flood hazard (overflowing/overwashing/overtopping).

The magnitude of observed IG waves during common storms at this large-scale inlet does not differ significantly from values reported in previous studies conducted on smaller inlets. However, the specific morphological characteristics of the inlet control IG wave reflection and amplification in the inner part of the inlet through resonance with the local bay-shaped coastline. As results, in the inner part of the inlet, the higher IG wave are observed at the sheltered coast.

IG wave contribution to TWL in large-scale inlet must be further investigated and integrated into directives addressing coastal risk in general and flood risk in particular. Otherwise, ignoring this process can

lead to a considerable underestimate of flood hazard in this environment.

CRediT authorship contribution statement

Alexandre Nicolae Lerma: Writing – original draft, Supervision, Resources, Project administration, Methodology, Investigation, Funding acquisition, Data curation, Conceptualization. **Nico Valentini:** Writing – review & editing, Validation, Software, Methodology, Investigation. **Paul Bayle:** Writing – review & editing, Validation, Methodology, Investigation, Data curation, Conceptualization. **Xavier Bertin:** Writing – review & editing, Methodology, Conceptualization. **Florian Ganthy:** Supervision, Funding acquisition. **Arnaud Le Pevedic:** Writing – review & editing, Data curation. **Guillaume Detandt:** Data curation. **Nadia Sénéchal:** Writing – review & editing, Funding acquisition.

Declaration of competing interest

The authors declare that they have no known competing financial interests or personal relationships that could have appeared to influence the work reported in this paper.

Data availability

Data will be made available on request.

Acknowledgments

This research is part of the ARCADE project and was co-funded by the Region Nouvelle-Aquitaine, the Parc Naturel Marin du Bassin d'Arcachon, the Agence de l'Eau Adour-Garonne, the Syndicat Intercommunal du Bassin d'Arcachon, the Bureau de Recherches Géologiques et Minières (Brgm) and the Institut Français de Recherche pour l'Exploitation de la Mer (Ifremer). The authors would like to thank the Direction Départementale des Territoires et de la Mer 33, the Syndicat Intercommunal du Bassin d'Arcachon, and the Observatoire de la Côte Nouvelle-Aquitaine (OCNA) for kindly providing the topo-bathymetric datasets and finally the Reserve Naturel du Banc d'Arguin for providing material and logistical support during the field campaigns. Finally, we would like to thank the two anonymous reviewers, whose comments and requests for clarification have considerably improved the article.

References

Allard, J., Chaumillon, E., Féniès, H., 2009. A synthesis of morphological evolutions and Holocene stratigraphy of a wave-dominated estuary: the Arcachon lagoon, SW France. Continent. Shelf Res. 29 (8), 957–969.

Baumann, J., Chaumillon, E., Bertin, X., Schneider, J.L., Guillot, B., Schmutz, M., 2017. Importance of infragravity waves for the generation of washover deposits. Mar. Geol. 391, 20–35.

Bayle, P., Lerma, A.N., Bertin, X., Sénéchal, N., Ganthy, F., 2022. Characterisation of infragravity waves and their associated hydrodynamics processes in meso-macro tidal lagoon. Coastal Engineering Proceedings (37), 159, 159.

Bertin, X., Olabarrieta, M., 2016. Relevance of infragravity waves in a wave-dominated inlet. J. Geophys. Res.: Oceans 121 (8), 5418–5435.

Bertin, X., Fortunato, A.B., Oliveira, A., 2009. A modeling-based analysis of processes driving wave-dominated inlets. Continent. Shelf Res. 851 (29), 819–834. https://doi.org/10.1016/j.csr.2008.12.019.

Bertin, X., de Bakker, A., van Dongeren, A., Coco, G., André, G., Ardhuin, F., Bonneton, P., Bouchette, F., Castelle, B., Crawford, W.C., Davidson, M., Deen, M., Dodet, G., Guérin, T., Inch, K., Leckler, F., McCall, R., Muller, H., Olabarrieta, M., Roelvink, D., Ruessink, G., Sous, D., Stutzmann, E., Tissier, M., 2018. Ifragravity waves: from driving machanisms to impacts. Earth-Sciences Reviews 177, 774–799.

Bertin, X., Mendes, D., Martins, K., Fortunato, A.B., Lavaud, L., 2019. The closure of a shallow tidal inlet promoted by infragravity waves. Geophys. Res. Lett. 46 (12), 6804–6810.

Bertin, X., Martins, K., de Bakker, A., Chataigner, T., Guérin, T., Coulombier, T., de Viron, O., 2020. Energy transfers and reflection of infragravity waves at a dissipative beach under storm waves. J. Geophys. Res.: Oceans 125 (5), e2019JC015714.

Biesel, F., 1952. Équations générales au second ordre de la houle irrégulière. La Houille Blanche 7 (3), 372–376. https://doi.org/10.1051/lhb/1952033.

Blanchet, H., de Montaudouin, X., Chardy, P., Bachelet, G., 2005. Structuring factors and recent changes in subtidal macrozoobenthic communities of a coastal lagoon, Arcachon Bay (France). Estuar. Coast Shelf Sci. 64 (4), 561–576.

Bruun, P., Gerritsen, F., 1959. Natural by-passing of sand at coastal inlets. J. Waterw. Harb. Div. 85 (4), 75–107.

Burvingt, O., Lerma, A.N., Lubac, B., Mallet, C., Senechal, N., 2022. Geomorphological control of sandy beaches by a mixed-energy tidal inlet. Mar. Geol. 450, 106863.

Capo, S., Lubac, B., Marieu, V., Robinet, A., Bru, D., Bonneton, P., 2014. Assessment of the decadal morphodynamic evolution of a mixed energy inlet using ocean color remote sensing. Ocean Dynam. 64, 1517–1530.

Carter, R.W.G., Woodroffe, C.D., 1994. Coastal Evolution: Late Quaternary Shoreline Morphodynamics. Cambridge University Press, p. 517.

Castelle, B., Bujan, S., Ferreira, S., Dodet, G., 2017. Foredune morphological changes and beach recovery from the extreme 2013/2014 winter at a high-energy sandy coast. Mar. Geol. 385, 41–55.

Castelle, B., Guillot, B., Marieu, V., Chaumillon, E., Hanquiez, V., Bujan, S., Poppeschi, C., 2018. Spatial and temporal patterns of shoreline change of a 280-km high-energy disrupted sandy coast from 1950 to 2014: SW France. Estuar. Coast Shelf Sci. 200, 212–223.

Cayocca, F., 2001. Long-term morphological modeling of a tidal inlet: the Arcachon Basin, France. Coast Eng. 42 (2), 115–142.

Chen, J.-L., Hsu, T.-J., Shi, F., Raubenheimer, B., Elgar, S., 2015. Hydrodynamic and sediment transport modeling of New River Inlet (NC) under the interaction of tides and waves. J. Geophys. Res. Oceans 120, 4028–4047.

Dachary-Bernard, J., Lyser, S., 2016. Aménités et hétérogénéité des préférences en matière d'aménagement du littoral: Le cas des touristes sur le bassin d'Arcachon. Économie Régionale et Urbaine (4), 847–876.

Daly, C.J., Bryan, K.R., Roelvink, J.A., Klein, A.H.F., Hebbeln, D., Winter, C., 2011. Morphodynamics of embayed beaches: the effect of wave conditions. J. Coast Res. 1003–1007.

De Beer, A.F., McCall, R.T., Long, J.W., Tissier, M.F.S., Reniers, A.J.H.M., 2021. Simulating wave runup on an intermediate–reflective beach using a wave-resolving and a wave-averaged version of XBeach. Coast Eng. 163, 103788.

de Montaudouin, X., Audemard, C., Labourg, P.J., 1999. Does the slipper limpet (Crepidula fornicata, L.) impair oyster growth and zoobenthos biodiversity? A revisited hypothesis. J. Exp. Mar. Biol. Ecol. 235 (1), 105–124.

Dodet, G., Bertin, X., Bruneau, N., Fortunato, A.B., Nahon, A., Roland, A., 2013. Wave–current interactions in a wave-dominated tidal inlet. J. Geophys. Res. Oceans 118, 1587–1605.

Dodet, G., Bertin, X., Bouchette, F., Gravelle, M., Testut, L., Wöppelmann, G., 2019. Characterization of sea-level variations along the metropolitan coasts of France: waves, tides, storm surges and long-term changes. J. Coast Res. (88), 10–24. Special Issue No.

Duong, T.M., Ranasinghe, R., Walstra, D., Roelvink, D., 2016. Assessing climate change impacts on the stability of small tidal inlet systems: why and how? Earth Sci. Rev. 154, 369–380.

Elgar, S., Herbers, T.H.C., Okihiro, M., Oltman-Shay, J., Guza, R.T., 1992. Observations of infragravity waves. J. Geophys. Res.: Oceans 97 (C10), 15573–15577.

Elias, E.P., Hansen, J.E., 2013. Understanding processes controlling sediment transports at the mouth of a highly energetic inlet system (San Francisco Bay, CA). Mar. Geol. 345, 207–220.

Fiedler, J.W., Smit, P.B., Brodie, K.L., McNinch, J., Guza, R.T., 2018. Numerical modeling of wave runup on steep and mildly sloping natural beaches. Coast Eng. 131, 106–113.

FitzGerald, D.M., Penland, S., Nummedal, D., 1984. Control of barrier island shape by inlet sediment bypassing: east Friesian Islands, West Germany. Mar. Geol. 60 (1–4), 355–376.

Fortunato, A.B., Freire, P., Mengual, B., Bertin, X., Pinto, C., Martins, K., et al., 2021. Sediment dynamics and morphological evolution in the Tagus Estuary inlet. Mar. Geol. 440, 106590.

Gallien, T.W., Kalligeris, N., Delisle, M.P.C., Tang, B.X., Lucey, J.T., Winters, M.A., 2018. Coastal flood modeling challenges in defended urban backshores. Geosciences 8 (12), 450.

Guza, R.T., Thornton, E.B., 1982. Swash oscillations on a natural beach. J. Geophys. Res. 87 (C1), 483–491.

Hanslow, D.J., Nielsen, P., Hibbert, K., 1996. Wave setup at river entrances. In: Coastal Engineering, pp. 2244–2257.

Hayes, M.O., 1979. Barrier island morphology as a function of tidal and wave regime. In: Leatherman, S. (Ed.), Barrier Islands, from the Gulf of St. Lawrence to the Gulf of Mexico. Academic, New York, pp. 1–27.

Hayes, M.O., FitzGerald, D.M., 2013. Origin, evolution, and classification of tidal inlets. J. Coast Res. 69 (10069), 14–33.

Idier, D., Castelle, B., Charles, E., Mallet, C., 2013. Longshore sediment flux hindcast : spatio-temporal variability along the SW Atlantic coast of France. J. Coast Res. 165, 1785–1790.

Janssen, T.T., Battjes, J.A., van Dongeren, A.R., 2003. Long waves induced by short-wave groups over a sloping bottom. J. Geophys. Res. 108, 3252. https://doi.org/10.1029/2002JC001515.

Lashley, C.H., Bertin, X., Roelvink, D., Arnaud, G., 2019. Contribution of infragravity waves to run-up and overwash in the pertuis Breton embayment (France). J. Mar. Sci. Eng. 7 (7), 205.

Lavaud, L., Bertin, X., Martins, K., Arnaud, G., Bouin, M.N., 2020. The contribution of short-wave breaking to storm surges: the case Klaus in the Southern Bay of Biscay. Ocean Model. 156, 101710.

Li, S., Liao, Z., Liu, Y., Zou, Q., 2020. Evolution of infragravity waves over a shoal under nonbreaking conditions. J. Geophys. Res. Oceans 125. https://doi.org/10.1029/2019jc015864 e2019JC015 864.
Liao, Z., Li, S., Liu, Y., Zou, Q., 2021. An analytical spectral model for infragravity waves over topography in intermediate and shallow water under nonbreaking conditions. J. Phys. Oceanogr. 51 (9), 2749–2765.
List, J.H., 1992. A model for the generation of two-dimensional surf beat. J. Geophys. Res. Oceans 97, 5623–5635. https://doi.org/10.1029/91JC03147.
Longuet-Higgins, M.S., Stewart, R.W., 1962. Radiation stress and mass transport in gravity waves, with application to 'surf beats'. J. Fluid Mech. 13 (4), 481–504.
Martins, K., Bonneton, P., Michallet, H., 2021. Dispersive characteristics of non-linear waves propagating and breaking over a mildly sloping laboratory beach. Coast Eng. 167, 103917.
McCall, R.T., De Vries, J.V.T., Plant, N.G., Van Dongeren, A.R., Roelvink, J.A., Thompson, D.M., Reniers, A.J.H.M., 2010. Two-dimensional time dependent hurricane overwash and erosion modeling at Santa Rosa Island. Coast Eng. 57 (7), 668–683.
Melito, L., Postacchini, M., Sheremet, A., Calantoni, J., Zitti, G., Darvini, G., et al., 2020. Hydrodynamics at a microtidal inlet: analysis of propagation of the main wave components. Estuar. Coast Shelf Sci. 235, 106603.
Mendes, D., Pinto, J.P., Pires-Silva, A.A., Fortunato, A.B., 2018. Infragravity wave energy changes on a dissipative barred beach: a numerical study. Coast Eng. 140, 136–146.
Mendes, D., Fortunato, A.B., Bertin, X., Martins, K., Lavaud, L., Silva, A.N., Pires-Silva, A., Thibault, Coulombier d., Coulombier, T., Pinto, J.P., 2020. Importance of infragravity waves in a wave-dominated inlet under storm conditions. Continent. Shelf Res. 192, 104026.
Mengual, B., Bertin, X., Place, F., Pezerat, M., Coulombier, T., Mendes, D., Fortunato, A. B., 2022. Wave-current interactions at the Tagus Estuary Mouth (Portugal) under storm wave conditions. Ocean Model. 175, 102035.
Mouragues, A., Bonneton, P., Castelle, B., Martins, K., 2021. Headland rip modelling at a natural beach under high-energy wave conditions. J. Mar. Sci. Eng. 9 (11), 1161.
Mugica, J., Paris, F., Nicolae Lerma, A., Pedreros, R., Ayache, B., Garcin, M., Bulteau, T., Hoareau, A., 2016. Caractérisation de l'aléa submersion marine dans le cadre des PPRL du Bassin d'Arcachon – Approche dynamique avec prise en compte des ouvrages de protection côtière. Dossier cartographique. BRGM/RP-64807-FR 324, 18 ann., 1 CD.
Muller, H., Van Rooijen, A., Idier, D., Pedreros, R., Rohmer, J., 2017. Assessing storm impact on a French coastal dune system using morphodynamic modeling. J. Coast Res. 33 (2), 254–272.
Nahon, A., Idier, D., Senechal, N., Féniès, H., Mallet, C., Mugica, J., 2019. Imprints of wave climate and mean sea level variations in the dynamics of a coastal spit over the last 250 years: Cap Ferret, SW France. Earth Surf. Process. Landforms 44 (11), 2112–2125.
Nahon, A., Idier, D., Bertin, X., Guérin, T., Marieu, V., Sénéchal, N., Mugica, J., 2022. Modelling the contribution of wind waves to Cap Ferret's updrift erosion. Coast Eng. 172, 104063.
Nahon, A., Fortunato, A.B., Oliveira, F.S., Azevedo, A., Henriques, M.J., Silva, P.A., et al., 2023. 2DH modelling and mapping of surfbeat-driven flooding in the shadow of a jettied tidal inlet. Coast Eng. 104342.
Nicolae Lerma, A.N., Bulteau, T., Lecacheux, S., Idier, D., 2015. Spatial variability of extreme wave height along the Atlantic and channel French coast. Ocean Eng. 97, 175–185.
Nicolae Lerma, A.N., Bulteau, T., Muller, H., Decarsin, C., Gillet, R., Paris, F., et al., 2018a. Towards the development of a storm erosion EWS for the French aquitaine coast. J. Coast Res. (85), 666–670.
Nicolae Lerma, A., Bulteau, T., Elineau, S., Paris, F., Durand, P., Anselme, B., Pedreros, R., 2018b. High-resolution marine flood modelling coupling overflow and overtopping processes: framing the hazard based on historical and statistical approaches. Nat. Hazards Earth Syst. Sci. 18 (1), 207–229.
Nicolae Lerma, A., Pedreros, R., Robinet, A., Sénéchal, N., 2017. Simulating wave setup and runup during storm conditions on a complex barred beach. Coast Eng. 123, 29–41.
Nicolae Lerma, A.N., Valentini, N., Bayle, P., Ganthy, F., Bertin, X., 2022. Contribution of infragravity waves to storm water level along a large inlet: implications for flooding and overtopping hazards. In: ICCE 2022-37th International Conference on Coastal Engineering.
Oh, S., Jung, J.H., Cho, S.K., 2020. Higher-order spectral method for regular and irregular wave simulations. J. Ocean Eng. and Technol. 34 (6), 406–418.
Olabarrieta, M., Warner, J.C., Kumar, N., 2011. Wave–current interaction in willapa bay. J. Geophys. Res. Oceans 116.
Orescanin, M.M., Elgar, S., Raubenheimer, B., 2016. Changes in bay circulation in an evolving multiple inlet system. Continent. Shelf Res. 124, 13–22.
Paniagua-Arroyave, J.F., Adams, P.N., Parra, S.M., Valle-Levinson, A., 2019. Observations of surface-gravity-wave scattering and dissipation by an isolated shoal related to a cuspate foreland. Continent. Shelf Res. 173, 43–55. https://doi.org/10.1016/j.csr.2018.12.004.
Pineau-Guillou, Lucia, 2013. PREVIMER. Validation des atlas de composantes harmoniques de hauteurs et courants de marée. ODE/DYNECO/PHYSED/2013-02.
Plus, M., Dumas, F., Stanisière, J.Y., Maurer, D., 2009. Hydrodynamic characterization of the Arcachon Bay, using model-derived descriptors. Continent. Shelf Res. 29 (8), 1008–1013.
Priestley, M.B., 1981. Spectral Analysis and Time Series (No Title).
Psuty, N.P., Ofiara, D.D., 2002. Coastal Hazard Management: Lessons and Future Directions from. Rutgers University Press, New Jersey.
Rabinovich, A.B., 2009. Seiches and harbor oscillations. In: Kim, Y.C. (Ed.), Handbook of Coastal and Ocean Engineering. World Scientific Publ., pp. 193–236
Rijnsdorp, D.P., Smit, P.B., Zijlema, M., 2014. Non-hydrostatic modelling of infragravity waves under laboratory conditions. Coast Eng. 85, 30–42.
Rijnsdorp, D.P., Smit, P.B., Guza, R.T., 2022. A nonlinear, non-dispersive energy balance for surfzone waves: infragravity wave dynamics on a sloping beach. J. Fluid Mech. 944, A45.
Roelvink, J.A., 1993. Dissipation in random wave groups incident on a beach. Coast Eng. 19 (1–2), 127–150.
Roelvink, D., Reniers, A., Van Dongeren, A.P., de Vries, J.V.T., McCall, R., Lescinski, J., 2009. Modelling storm impacts on beaches, dunes and barrier islands. Coast Eng. 56 (11–12), 1133–1152.
Roelvink, D., McCall, R., Mehvar, S., Nederhoff, K., Dastgheib, A., 2018. Improving predictions of swash dynamics in XBeach: the role of groupiness and incident-band runup. Coast Eng. 134, 103–123.
Ruessink, B.G., Kleinhaus, M.G., van den Beukel, P.G.L., 1998. Observations of swash under highly dissipative conditions. J. Geophys. Res. 103 (C2), 3111–3118.
Ruggiero, P., Komar, P.D., McDougal, W.G., Marra, J.J., Beach, R.A., 2001. Wave runup, extreme water levels and the erosion of properties backing beaches. J. Coast Res. 407–419.
Ruggiero, P., Holman, R.A., Beach, R.A., 2004. Wave run-up on a high-energy dissipative beach. J. Geophys. Res. 109 (C6), C06109.
Ruju, A., Lara, J.L., Losada, I.J., 2012. Radiation stress and low-frequency energy balance within the surf zone: a numerical approach. Coast Eng. 68, 44–55.
Russell, P.E., 1993. Mechanisms for beach erosion during storms. Continent. Shelf Res. 13 (11), 1243–1265.
Sacareau, I., 2018. Entre attractivité touristique et attractivité résidentielle: quelles dynamiques spatiales du tourisme sur le bassin d'Arcachon?. Sud-Ouest européen. Rev. Geogr. Pyrenees Sud-Ouest (45), 39–51.
Salles, P., Valle-Levinson, A., Sottolichio, A., Senechal, N., 2015. Wind-driven modifications to the residual circulation in an ebb-tidal delta: Arcachon L agoon, S outhwestern F rance. J. Geophys. Res.: Oceans 120 (2), 728–740.
Senechal, N., Sottolichio, A., Bertrand, F., Goeldner-Gianella, L., Garlan, T., 2013. Observations of waves'impact on currents in a mixed-energy tidal inlet : Arcachon on the southern French Atlantic coast. J. Coast Res. SI65, 2053–2058.
Stockdon, H.F., Holman, R.A., Howd, P.A., Sallenger, A.H., 2006. Empirical parameterization of setup, swash, and runup. Coast. Eng. 53 (7), 573–588.
Stockdon, H.F., Thompson, D.M., Plant, N.G., Long, J.W., 2014. Evaluation of wave runup predictions from numerical and parametric models. Coast Eng. 92, 1–11.
Svendsen, I.A., 2005. Introduction to Nearshore Hydrodynamics, vol. 24. World Scientific Publishing Company.
Van Leeuwen, P.J., 1992. Low frequency wave generation due to breaking waves. Ph.D. dissertation. Delft University of Technology, p. 151.
Velasquez-Montoya, L., Overton, M.F., Sciaudone, E.J., 2020. Natural and anthropogenic-induced changes in a tidal inlet: morphological evolution of Oregon Inlet. Geomorphology 350, 106871.
Vila-Concejo, A., Matias, A., Pacheco, A., Ferreira, Ó., Dias, J.A., 2006. Quantification of inlet-related hazards in barrier island systems. An example from the Ria Formosa (Portugal). Continent. Shelf Res. 26 (9), 1045–1060.
Wargula, A., Raubenheimer, B., Elgar, S., 2014. Wave-driven along-channel subtidal flows in a well-mixed ocean inlet. J. Geophys. Res.: Oceans 119 (5), 2987–3001.
Williams, M.E., Stacey, M.T., 2016. Tidally discontinuous ocean forcing in bar-built estuaries: the interaction of tides, infragravity motions, and frictional control. J. Geophys. Res.: Oceans 121 (1), 571–585.
Zippel, S., Thomson, J., 2015. Wave breaking and turbulence at a tidal inlet. J. Geophys. Res.: Oceans 120, 1016–1031.